Design and Characterization of InGaAsP/InP and In(Al)GaAsSb/GaSb Laser Diode Arrays

A Dissertation Presented

by

Alexandre Gourevitch

to

The Graduate School

in Partial fulfillment of the

Requirements

for the Degree of

Doctor of Philosophy

in

Electrical Engineering

Stony Brook University

May 2006

Abstract of the Dissertation

Design and Characterization of InGaAsP/InP and In(Al)GaAsSb/GaSb Laser Diode Arrays

by

Alexandre Gourevitch

Doctor of Philosophy

in

Electrical Engineering

Stony Brook University
2006

Semiconductor laser diodes and laser diode arrays are efficient electrical to optical power converters providing their output energy in relatively narrow emission spectra. The different wavelength ranges are well covered by different semiconductor materials. InP-based laser diodes cover the wavelength range from 1-μm to 2-μm. The region between 2 and 3-μm is well handled by type-I devices based on the GaSb material system.

We designed, fabricated and characterized InP-based and GaSb-based laser arrays with record high continuous wave output power emitting at 1.5-μm and 2.3-μm, correspondingly. A laser array based on the InGaAsP/InP material system was developed for optical pumping of erbium doped solid state lasers emitting eye-safe light around 1.6-μm. The 2.3-μm laser arrays can be used for optical pumping of recently developed type-II semiconductor lasers operating in the mid-infrared atmospheric transparency window between 3.5-μm and 5-μm.

Optical pumping requires pump sources that reliably provide output energy in a relatively narrow spectral range matching with absorption bands of illuminated materials. Also the compact size of laser diodes and laser arrays is preferable and convenient in different implementations, but it leads to significant overheating in high power operations. The inherent properties of semiconductor materials result in a red-shift of the laser emission spectrum with increased temperature. This thermal drift of the laser emission spectrum can lead to misalignment with the narrow absorption bands of illuminated materials. We have developed an experimental technique to measure the time-resolved evolution of the laser emission spectrum. The data obtained from the emission spectrum measurements have been used to optimize the laser device design.

In this dissertation the progress in the development of high-power infrared laser arrays have been discussed. The different aspects of laser array design, thermal analysis and laser bar optimization have been studied analytically and experimentally.

Table of Contents

List of Illustration v
List of Tables x
List of Publications xi
I. High power laser arrays 3
A. Introduction 3
B. Applications of 1.5-μm high-power laser arrays 6
C. Applications of 2.3-μm high-power laser arrays 9
II. Performance of infrared laser diodes 12
A. Introduction 12
B. Design and performance of 1.5-μm single lasers 13
C. Design and performance of 2.3-μm single lasers 17
D. Conclusion 24
III. Thermal resistance and optimal fill factor of a high power diode laser bar 25
A. Introduction 25
B. Optimal fill factor 28
C. Electric resistance of the bar 32
1. Potential distribution in n-layer 34
2. Potential at the active region 36
3. Calculation of the resistance 38
D. Thermal resistance 38
1. Planar geometry 39
2. Perpendicular geometry 41
E. Results and discussion 42
F. Conclusion 49
IV. Performance of infrared high-power laser diode arrays 50
A. Introduction 50
B. Design and performance of 1.5-μm laser arrays 51

C. Design and performance of 2.3-μm laser arrays 53
D. Steady-state thermal analysis of high-power laser arrays 56
E. Conclusion 60
V. Transient thermal analysis of high-power diode laser arrays with different fill factors 61
A. Introduction 61
B. Device structure and experimental technique 63
C. Theory 65
1. Vertical geometric model 65
2. Three heating periods 68
D. Results and discussion 71
E. Conclusion 76
F. Appendix (Vertical geometric model) 78
VI. References 82

List of Illustrations

FIG. 1: Schematic diagram of an edge emitting laser bar 2

FIG. 2: Absorption (blue line) and emission (red) for Er:YAG 6

FIG. 3: Schematic band diagram showing the energy gap sequence of two repetitions of an InAs/InGaSb/InAs active region, three repetitions of InGaAsSb integrated absorbers, and one clad layer. Dashed lines represent upper and lower lasing levels 8

FIG. 4: Schematic energy band diagram of the broadened waveguide 1.5-μm wavelength InGaAsP/InP laser. 12

FIG. 5: Continuous-wave output-power and conversion efficiency characteristics of 1.5-μm wavelength lasers. 13

FIG. 6: Pulse mode output-power characteristics of 1 mm long and 100 μm wide single laser operating at 1.5-μm wavelength. 13

FIG. 7: Temperature dependencies of the threshold current, and the external quantum efficiency, for 1-mm-long laser measured in the pulsed regime. 14

FIG. 8: Schematic energy band diagram of the broadened waveguide 2.3-μm wavelength In(Al)GaAsSb/GaSb laser. 16

FIG. 9: Continuous-wave output-power and conversion efficiency characteristics of 2.3-μm wavelength lasers. 18

FIG. 10: Pulse mode output-power characteristics of 1 mm long and 100 μm wide single laser operating at 1.5-μm wavelength. 19

FIG. 11: Temperature dependencies of the threshold current, and the external quantum efficiency, for 1-mm-long laser measured in the pulsed regime. 19

FIG. 12: Laser spectra of 2.3-μm wavelength lasers measured at several temperatures in pulsed (left) and CW (right) operation. 20

FIG. 13: Perspective views of the mounted laser bar. (a) The planar model with the laser bar, heat spreader and heat sink describing parallel planes. Light is emitted from the electrically pumped active regions defined by the multiple p-contacts of width a. The center-to-center distance between p-contacts is a1, and the thickness of the heat spreader is d. A detailed view of the laser bar is shown in the circular inset. The inset shows that the laser bar consists of an n-layer (n-cladding and substrate) of thickness b, a thin active region and a p-clad of thickness b1. Different coordinate systems have been used. The electrical resistance modeling employs the coordinate origin shown in the inset, the thermal resistance modeling employs the coordinate origin shown in the main drawing. (b) The perpendicular model with a similar laser bar mounted in a grooved heat spreader. The laser bar cavity length L and heat spreader thickness D are shown in the inset. The asymmetry of the n and p layer thicknesses means that the heat transfer is through the p-side of the bar which is modeled as a planar heat source of negligible thickness. 28

FIG. 14: Measured overheating of the active region versus dissipated power density p_{dis} (a) for different fill factor laser bars with 1 mm long cavities mounted in BeO heat spreaders and (b) for different fill factor laser bars with 2 mm long cavities mounted in CuW heat spreaders. Solid symbols indicate data points (circles, squares, and triangles for 10%, 20%, and 40% fill factors

respectively). Lines fit to the experimental data are used to determine the thermal resistance. 44

FIG. 15: Optimized fill factor (dashed line) and corresponding maximum output power (solid line) as a function of laser temperature rise. 45

FIG. 16: Optimized fill factor (dashed line) and corresponding minimal laser temperature rise (solid line) as a function of output power. The dotted lines show the temperature rise for several fixed fill factor arrays as a function of output power. 46

FIG. 17: Output power (circles) and wall-plug efficiency (squares) of a 1.5-μm 1-D array operated in q-CW (open symbols) and CW (closed symbols) modes at a coolant temperature of 16 ^{o}C. Inset demonstrates integrated emission spectrum of the array measured at 40 A and 18 ^{o}C. 50

FIG. 18: Output power of a 2-D array operated in the q-cw mode at 18 ^{o}C. Inset demonstrates integrated emission spectrum of a 2-D array recorded at 40 A and 18 ^{o}C. 52

FIG. 19: Current characteristics of output-power and wall-plug efficiency of 2.3-μm laser linear array. The light-current characteristics in cw and q-cw were measured at 18 ^{o}C coolant temperature and at room temperature (uncooled) in short pulse operation. The inset shows the laser array emission spectrum measured at 30-A drive current and 18 ^{o}C coolant temperature in CW operation. 53

FIG. 20: The experimentally measured active-region temperature rise as a function of dissipated power is shown for different fill factor arrays. The inset shows the dependence of the thermal resistance on fill factor. 56

FIG. 21: Active-region temperature distribution over 1 mm of a 1cm long laser bar with different fill factors at the total dissipated power of 20 W. The inset demonstrates the analytical (solid symbols) and experimental (open symbols) average temperature change for different FFs at given total dissipated power of 20 W. 57

FIG. 22: Time dependence of average wavelength shift (left axis) and the corresponding active region temperature change (right axis) for a laser diode array with a 20% fill factor. 63

FIG. 23: Active region temperature rise divided by dissipated power (i.e. thermal resistance) as a function of time for different FF arrays. 64

FIG. 24: The cross section geometry of the laser array assembly used for the calculation of the temperature distribution is shown. The BeO heat spreader occupies the region $0 < y < b$. The laser bar is plotted by the line A-B. The interface between the BeO heat spreader and the heat sink lies at $y = b$. 65

FIG. 25: The Active-region initial temperature rise during the first 200 μs for 10%, 20%, and 40% FF arrays at a constant total bar P_{dis} of 25 W. 68

FIG. 26: The temperature changes are plotted on double-log axes for the three fill factors. The solid lines were fitted to the experimental data over the time interval of 200 μs to 10 ms. The computed slopes are shown in the inset as a function of the fill factor. 70

FIG. 27: The active-region temperature change of a 20% fill factor array is plotted vs the square-root of time with 30-, 40-, and 50-A drive currents at a coolant temperature of 18 ^{o}C. The dependency of the slope coefficient α the total

dissipated power is shown for 10% (square symbol), 20% (circle symbol), and 40% (triangle symbol) fill factor arrays in the inset. 71

FIG. 28: Normalized deviation from steady-state temperature vs time is plotted for arrays with 10%, 20%, and 40% FF. The slopes of the solid lines are used to calculate τc, which is shown in the inset. 73

List of Tables

TABLE I. InGaAsP/ InP laser heterostructure. 15
TABLE II. In(Al)GaAsSb/ GaSb laser heterostructure. 21

List of Publications:

Refereed Journals:

1. B. Laikhtman, A. Gourevitch, D. Westerfeld, D. Donetsky and G. Belenky, "Thermal resistance and optimal fill factor of high power laser bar", *Semicond. Sc. Technol*. 20, 1087-1095, (2005).
2. A. Gourevitch, B. Laikhtman, D. Westerfeld, D. Donetsky, G. Belenky, C. W. Trussell, Z. Shellenbarger, H. An, R. U. Martinelli, "Transient thermal analysis of InGaAsP-InP high-power diode laser arrays with different fill factors", *J. Appl. Phys.*, 97, 084503 1-6, (2005).
3. L. Shterengas, G.L. Belenky, A. Gourevitch, D. Donetsky, J.G. Kim, R.U. Martinelli, and D. Westerfeld, "High power 2.3-μm GaSb-based linear laser array", *IEEE Photon. Tech. Lett.* 16, 2218-2220, (2004)
4. G. Belenky, J.G. Kim, L. Shterengas, A. Gourevitch, R.U. Martinelli, "High-power 2.3-μm laser arrays emitting 10 W CW at room temperature", *Electron. Lett*., 40, 737-738, (2004)
5. B. Laikhtman, A. Gourevitch, D. Donetsky, D. Westerfeld, G. Belenky, "Current spread and overheating of high power laser bars", *J. Appl. Phys*., 95, 3880-3889, (2004)
6. A. Gourevitch, G. Belenky, D. Donetsky, B. Laikhtman, D. Westerfeld, C.W. Trussell, H. An, Z. Shellenbarger, R. Martinelli, "1.47-1.49-μm InGaAsP/InP diode laser arrays", *Appl. Phys. Lett*., 83, 617-619, (2003)
7. L. Shterengas, G.L. Belenky, A. Gourevitch A, J.G. Kim, R.U. Martinelli, "Measurements of alpha-factor in 2-2.5 μm type-I In(Al)GaAsSb/GaSb high power diode lasers", *Appl. Phys. Lett.,* 81, 4517-4519 (2002)

Conference Proceedings:

8. A. Gourevitch, G. Belenky, L. Shterengas, D. Donetsky, D. Westerfeld, B. Laikhtman, R.U. Martinelli, G. Kim, "1.5 and 2.3-μm Diode Laser Arrays for Optical Pumping", Optics & Photonics 2005, co-located with the SPIE 50th Annual Meeting, Proceedings of SPIE Volume: 5887, pp. 239-247, 2005
9. A. Gourevitch, D. Donetsky, G. Belenky B. Laikhtman, D. Westerfeld, Z. Shellenbarger, H. An, R. U. Martinelli, C. W. Trussell, "Transient thermal analysis of 1.47-μm high power diode laser arrays", Proceeding of the Solid State and Diode Laser Technology Review, SSDLTR-04, P-9, 2004.
10. G. Belenky, L. Shterengas, A. Gourevitch, D. Donetsky, J. Kim, R. U. Martinelli, D. Westerfeld, "2.3-μm GaSb-based diode laser linear arrays emitting 10W CW at room temperature", Proceeding of the Solid State and Diode Laser Technology Review, SSDLTR-04, P-20, 2004.
11. G. Belenky, A. Gourevitch, D. Donetsky, D. Westerfeld, B. Laikhtman, C.W. Trussell, H. An, Z. Shellenbarger, R. Martinelli, "1D and 2D 1.5-μm InGaAsP-InP diode laser arrays: experiment and modeling", Proceeding of Lasers and Electro-Optics, CLEO 03, 432-434, 2003.
12. G. Belenky, A. Gourevitch, D. Donetsky, D. Westerfeld, C. W. Trussell, H. An, Z. Shellenbarger, R. Martinelli, "High power 1.5-μm InGaAsP-InP Diode Laser Arrays", Proceeding of the Solid State and Diode Laser Technology Review, SSDLTR-03, P-10, 2003.
13. L.Shterengas, A.Gourevich, G.Belenky, J.G.Kim, R.Martinelli, "Measurements of alpha-factor in 2-2.5-μm type-I In(Al)GaAsSb/GaSb broadened waveguide lasers", Lasers and Electro-Optics, CLEO 2002. Technical Digest., pp. 157 - 158 vol.1, 2002

I. HIGH POWER LASER ARRAYS

A. Introduction

The remarkable improvement of high-power diode lasers makes them very attractive for different applications, like material processing, optical pumping, secure free-space communication and infrared countermeasures. The key requirements for successful commercialization of high-power laser diodes are high output power, high efficiency, reliable operation, and low fabrication cost.

One basic approach for higher output power is to enlarge the laser diode gain area: increase the stripe width (emitting aperture) and/or cavity length. However, this approach encounters optical field filamentation and lateral mode instabilities, leading to the appearance of so-called hot spots and the degradation of the laser. Usually, the width of a single emitter does not exceed 200 μm.

Another way to increase the gain area is to increase the number of emitters integrated side by side on a monolithic laser bar. These emitters are electrically connected in parallel, and are optically isolated from each other. Figure 1 shows a section of such a laser bar. The output power from laser bar scales with the number of emitters, so each stripe can emit a moderate output power which does not cause facet degradation. Today, commercially available high-power diode laser arrays demonstrate output powers up to 100 W from a single bar [1–5]. Higher output powers up to the kW-regime are obtained from stacked arrays of these bars [6–8].

The integration of laser emitters in a monolithic bar implies some crucial prob-

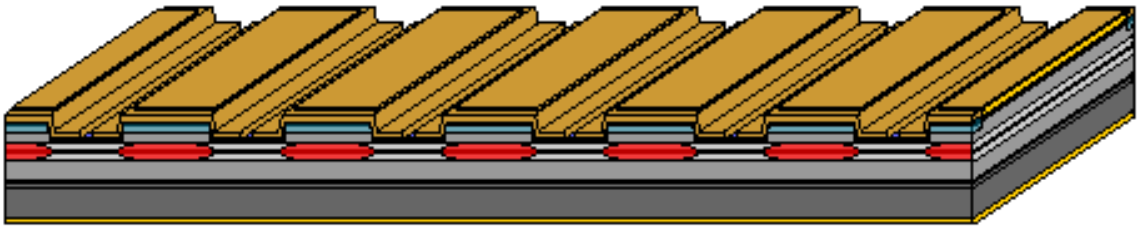

FIG. 1: Schematic diagram of an edge emitting laser bar.

lems: 1) technological problems 2) spurious modes 3) high heat dissipation in a relatively small volume 4) mutual heating of adjacent emitters.

The technological steps to process the laser diode bar are similar to the ones for single laser diode, the difference is only in the mask layout. However, each process step must be carried out to a very high reliability level. A defect of one emitter can cause the failure of the entire bar by electrical or thermal effects.

Another problem arising from the integration of broad area emitters is the appearance of so-called spurious modes that decrease the overall output power from the laser bar. These modes have a propagation direction perpendicular to the desired output. These parasitic modes appear in bars with a high fill factor, and have to be suppressed by increasing the optical losses for such modes. The filling factor is the ratio of the active (pumped) area to the whole area of the laser bar. There are several approaches to suppress spurious modes. One approach is to etch deep grooves between the emitters. Another approach is to use the etched mesa structure itself to create an asymmetric optical field distribution for parasitic modes, resulting in high optical leakage from the waveguide layers into the substrate.

Recently, some groups sponsored by the Defense Advanced Research Projects Agency (DARPA) Super High Efficiency Diode Sources (SHEDS) Program demon-

strated record high peak power conversion efficiencies approaching 70% [1, 2, 9, 10]. Conversion efficiency is defined as the ratio between output optical power (P_{out}) and input electrical power (P_{out}). Usually, the conversion efficiency varies significantly for laser diodes based on different semiconductor materials and is less than 50%. As a result, a considerable amount of heat is generated in diode lasers and laser bars during high-power operation. The relatively small size of diode laser bars results in a relatively high thermal resistance R_{th}, which is defined as the temperature rise of the active region divided by the dissipated power:

$$R_{th} = \frac{\Delta T}{P_{in} - P_{out}} \tag{1.1}$$

Depending on the thermal resistance, the heat dissipation in laser diodes results in an active region temperature rise. This temperature rise limits the output power (through so-called thermal rollover) and enhances the device degradation mechanisms. It is therefore critical to minimize the thermal resistance in high-power laser devices.

The close proximity of adjacent laser emitters results in an overlapping of heat fluxes from neighboring stripes. The overlapping of heat fluxes leads to an additional temperature rise due to mutual overheating of adjacent stripes [11, 12]. However, it was shown in Ref. [13] that the thermal resistance decreases with increased filling factor. A detailed analysis of fill factor influence on laser bar overheating is considered in chapter III.

In this dissertation, progress in the development of high-power infrared laser arrays is discussed, including the development of InP-based and GaSb-based laser

arrays operating at 1.5-μm and 2.3-μm, correspondingly. The different aspects of laser array design, thermal analysis and laser bar optimization have been studied analytically and experimentally.

B. Applications of 1.5-μm high-power laser arrays

Optically pumped erbium doped solid state lasers operating between the $^4I_{13/2}$ and $^4I_{15/2}$ laser transition are well suited for the production of high power eye-safe laser light between 1.5 - 1.65-μm. These lasers provide the combination of beam quality, efficiency, and high optical power required for different applications. Erbium doped solid state lasers are typically pumped at a wavelength between 940 and 980 nm ($\sim$ 1.3 eV/photon) and emit in the eye-safe region 1.5 - 1.65-μm ($\sim$0.8 eV/photon). The difference in energy between the pump light photons and the laser emission photons is known as the quantum defect, and represents energy that is lost to heat in the solid state laser. The quantum defect for our example laser is near 0.5 eV; at least 38% of the pumping optical power is wasted to heat due to the quantum defect alone.

This inefficiency is undesirable anywhere in the high power laser system, but it is particularly undesirable to apply high heat loads in the solid state laser medium. High temperatures in the solid state laser material limit both the output beam power and quality. A temperature gradient in the laser material leads to an index-of-refraction gradient which induces self-focusing and degrades beam quality. It may be possible to compensate for this index variation through advanced design, but this becomes increasingly difficult in the presence of thermal transients. Non-uniform

heating also introduces mechanical forces that can lead to crystal fractures. Finally, the solid state laser structure is poor from a heat transport perspective; the long path from the pumped region to the cooled periphery acts to virtually guarantee large temperature variations if the laser is pumped with a high quantum defect source. Various designs (e.g. the spinning disk solid state laser) have been proposed to address the heating problem, each with its own disadvantages.

There are more difficulties associated with high quantum defect solid state laser pumping schemes. One of these difficulties lies in the requirement for sensitizer atoms (typically ytterbium for erbium based lasers) to be co-doped into the solid state host material. These sensitizer atoms allow for efficient absorption of the relatively shortwave length pump light, but their use places constraints on the erbium concentration, which in turn constrains the gain, absorption and energy storage capability of the solid state laser.

Sensitizer atoms and a high quantum defect combine to facilitate up conversion, process whereby already excited dopant atoms absorb additional energy and enter very high energy states that do not contribute to the 1.5 - 1.65-μm laser emission. This process depletes the upper laser state population, while simultaneously wasting pump power and increasing host heating.

An alternative to high quantum defect pumping is to pump directly into the upper part of the narrow band of energies available to excited Erbuim atoms [14–19]. This near resonant pumping scheme requires high power laser diodes that can put a large fraction of their output energy in a fairly narrow energy band. This pump light spectral precision must be maintained over a range of diode operating

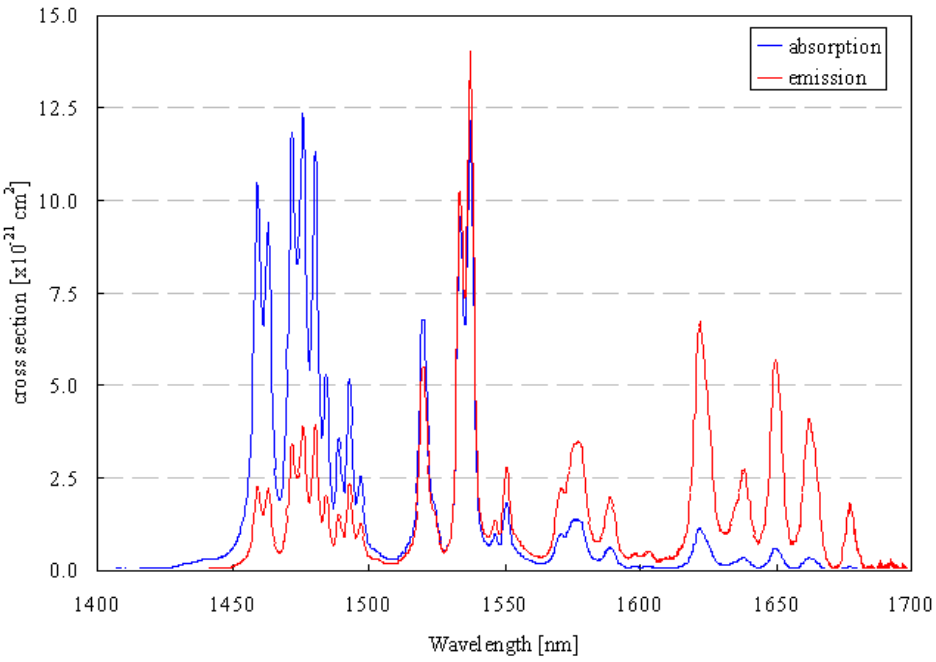

FIG. 2: Absorption (blue line) and emission (red) for Er:YAG

temperatures. Figure 2 shows the absorption and emission spectra for a Er:YAG laser material. In this material, absorption of pump light in the 1.47 - 1.49-μm region can be used to generate emission at 1.5 - 1.64-μm, for a quantum defect of only around 0.06 eV. Semiconductor sources can be tailored to deliver their energy into the spectral region required by the solid state laser designer. The material in Figure 2 can also be pumped at 1.52-μm for emission at 1.64-μm [17]. There are technical challenges for such a system, but the resulting quantum defect of only a few thousandths of an eV makes this approach very attractive. These quantum defects are two orders better than is obtained with traditional high quantum defect pumping methods.

C. Applications of 2.3-μm high-power laser arrays

Diode laser arrays operating in the spectral range 2 - 3-μm are promising as compact and efficient light emitters for different applications. Atmospheric transparency in the 2.0 - 2.4-μm region permits applications as diverse as secure free-space communication and infrared countermeasures (IRCM). Further, these lasers are ideally suited for use as pump sources for new solid state and optically pumped semiconductor sources operating in the mid-infrared atmospheric transparency windows between 3.5-μm and 5.0-μm.

Type-I GaSb-based semiconductor lasers operate up to 2.85-μm [20] and output hundreds of milliwatts in continuous-wave (CW) mode at room temperature [21–29]. These devices can be used as low quantum-defect pumping sources for a new generation of optically pumped semiconductor lasers operating in band-II of the atmospheric transparency [30]. High-power CW laser arrays based on InP material system were fabricated with the longest wavelengths of 1.9-μm (11 W per 1 cm bar) [31] and 2-μm (8.5 W per 1 cm bar) [32]. Further increasing the operating wavelength within the InP-based material system leads to dramatic laser performance degradation. The longest reported operating wavelength of the diode laser arrays was 2.05-μm achieved with In(Al)GaAsSb/GaSb material system [33] though the array was not designed to work in high-power CW regime.

As an example of the advantages of high-power 2.3-μm pump arrays, we will consider the 4-μm type-II lasers recently reported by the Air Force Research Laboratory [34]. As can be seen in Figure 3, these devices have an active region consisting of

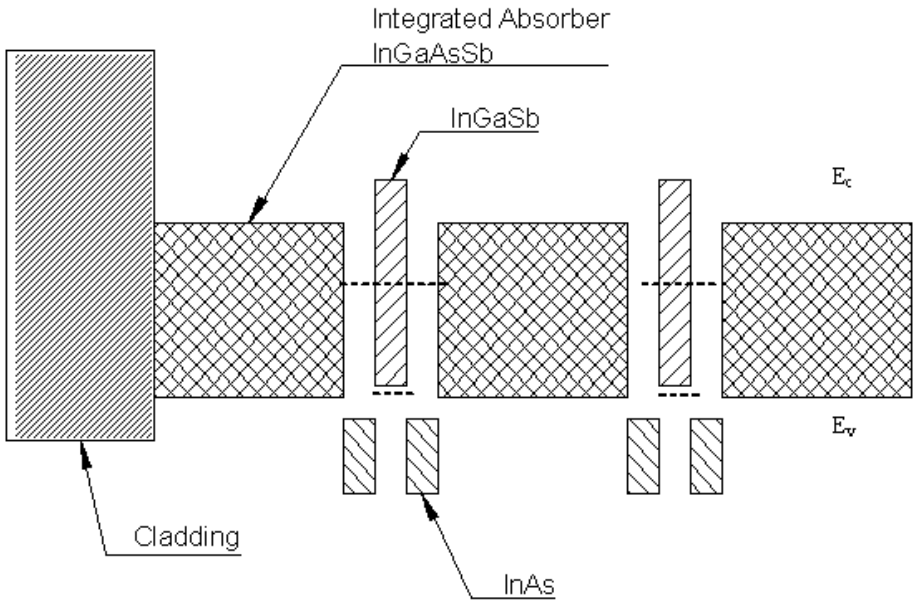

FIG. 3: Schematic band diagram showing the energy gap sequence of two repetitions of an InAs/InGaSb/InAs active region, three repetitions of InGaAsSb integrated absorbers, and one clad layer. Dashed lines represent upper and lower lasing levels

multiple layers of InAs and InGaSb sandwiched between integrated absorber (IA) layers of InGaAsSb. Light emission is due to transitions between electrons confined in the InAs wells and holes confined in the InGaSb wells [35]. Carriers are provided by absorption of pump radiation in the quaternary integrated absorber layers.

The alloy composition of the IA layers is chosen for lattice matching to the GaSb substrate, and also to provide an appropriate band gap for efficient absorption of the pump radiation. The energy difference between the pump photons and the emitted photons is known as the quantum defect, and this energy is dissipated by heating the laser structure.

Since device heating adversely affects the devices performance, it is desirable to minimize the quantum defect. Recently, type-II lasers have been pumped with 1.85-

μm laser light (0.67 eV pump photon energy). These type-II devices emit light at around 4.0-μm (0.31 eV), producing a quantum defect of 0.36 eV. The proposed 2.3-μm source emits photons with energy of 0.54 eV, yielding a quantum defect of just 0.23 eV. By switching from the 1.85-μm pump sources to 2.3-μm pump sources the quantum defect is reduced by 36%.

There are limits as to how much the quantum defect can be reduced in these structures. In particular, the edge of the miscibility gap for lattice matched GaInAsSb will cause problems in designing the IA for wavelengths much longer than 2.3-μm [36].

II. PERFORMANCE OF INFRARED LASER DIODES

A. Introduction

InGaAsP/InP is one of the basic material systems of modern optoelectronics. Well-developed metal organic chemical vapor deposition (MOCVD) technology allows for high yield fabrication of InP-based lasers in the wavelength range from 1-μm to 2-μm. The region between 2-μm and 3-μm is well handled by type-I laser devices based on the GaSb material system, grown by molecular beam epitaxy (MBE). Recently, lasers with continuous-wave operation up to 3.04-μm have been demonstrated [22, 38, 39]. These lasers comprise compressively strained GaInAsSb quantum wells (QWs) with indium concentrations up to 50% and lattice matched AlGaAsSb barriers and waveguides.

In this chapter we consider the details of laser heterostructure design of diode lasers operating at 1.5-μm and 2.3-μm wavelength. The design of both lasers is focused on high-power operations. That requires low threshold current and high efficiency. The common feature of both designs is a broadened-waveguide layer. The broadened waveguide (BW) approach reduces overlap of the optical field with highly doped cladding layers and minimizes the optical losses due to free carrier absorption [40]. This chapter is organized as follows. In section II B we present the design and performance details of InP-based single emitters. In section II C the design and performance of GaSb-based single lasers are considered.

B. Design and performance of 1.5-μm single lasers

The InGaAsP/InP laser structure emitting at 1.5-μm was grown by metalloorganic chemical vapor deposition. The schematic energy band-gap diagram of laser structure is shown on Figure 4. The active region contains three 6-nm InGaAsP quantum wells (QWs) with 1% compressive strain separated by 16-nm InGaAsP barriers. A double-step graded-index separate confinement heterostructure (SCH) with 300-nm-thick outer and 30-nm-thick inner InGaAsP layers provides optical confinement. The broadened waveguide (710 nm) was incorporated between n- and p-clad layers, each 1.5-μm thick. The n-cladding was doped with Se with a concentration of $5 * 10^{17} cm^{-3}$ and the p-cladding was gradually doped with Zn with an average concentration of $7.5 * 10^{17} cm^{-3}$. Zn doping of the p-cladding was optimized to exhibit optical losses as low as 2-3 cm^{-1} [41, 42]. All layers, the composition and thickness of which are given in Table I, except the QWs were grown lattice-matched to the InP substrate. The total thickness of the laser structure including the substrate was 140 μm. Details of the laser heterostructure design were reported elsewhere [41–44].

The wafer was processed into single emitters. The laser emitters had 100-μm stripe width, 1-mm and 2-mm cavity length. The laser facets were high-reflection/antireflection coated with reflection coefficients of 95% and 3%, respectively. These lasers were indium-soldered epi-side down onto copper heat sinks and were characterized.

Figure 5 shows CW current characteristics of output power and wall-plug effi-

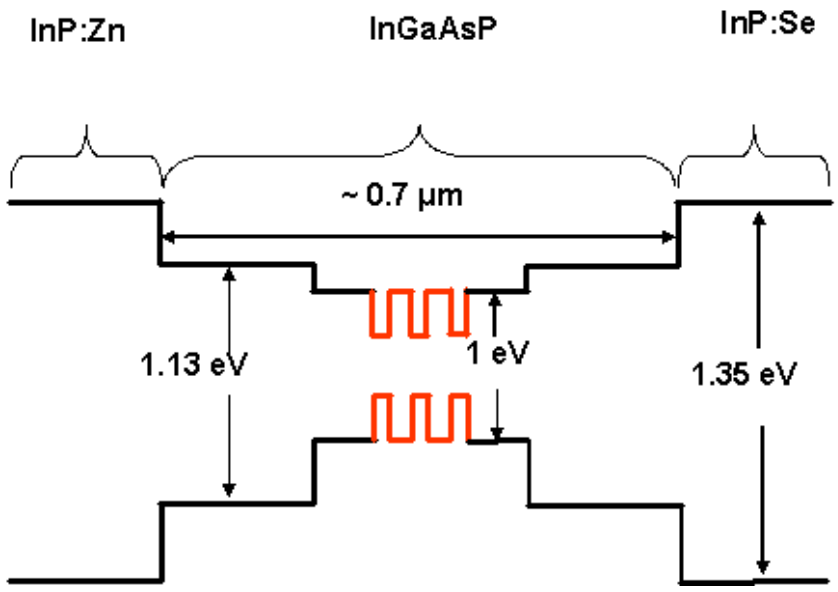

FIG. 4: Schematic energy band diagram of the broadened waveguide 1.5-μm wavelength InGaAsP/InP laser.

ciency for 1-mm and 2-mm-long single lasers, measured at a heat sink temperature of 18 C. The lasers output 1.2 W and 2.2 W in CW operation. The wall-plug efficiency of 28% and 30% peaked at 2 A and 3 A for the 1-mm and 2-mm-long single lasers, correspondingly. The far field radiation pattern was measured for a single laser at 1.5 A CW drive current. The fast axis divergence was 44^o FWHM, the slow divergence 8^o FWHM.

Figure 6 shows the performance of 100-μm-wide 1-mm-long single laser measured in pulse operation (200 ns, 1 MHz) at different heat sink temperatures. The threshold current density was around 480 A/cm^2 and a differential efficiency was 60 % at a 20 ^{o}C. Over the temperature range from 20 to 70 ^{o}C, the threshold characteristic temperature T_0 was 54 K and the slope-efficiency characteristic temperature T_1 was 160 K, Figure 7.

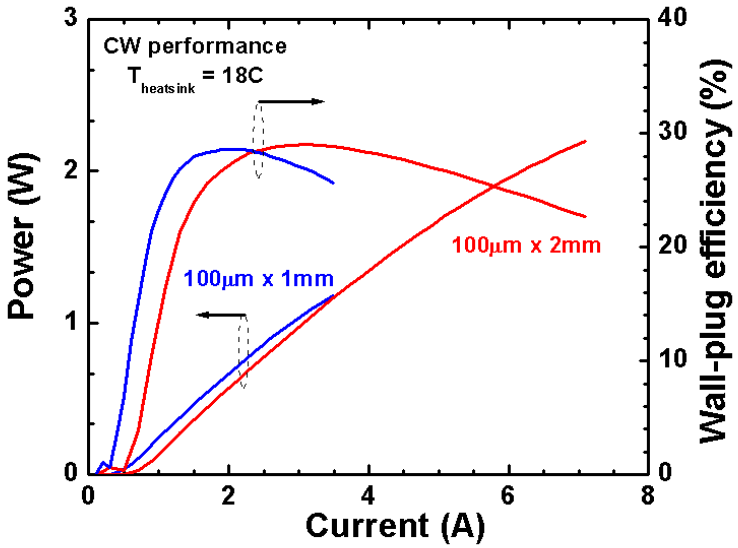

FIG. 5: Continuous-wave output-power and conversion efficiency characteristics of 1.5-μm wavelength lasers.

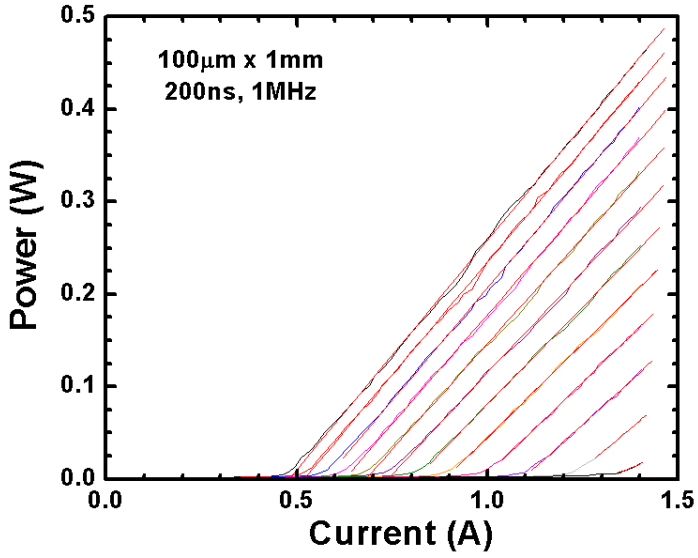

FIG. 6: Pulse mode output-power characteristics of 1 mm long and 100 μm wide single laser operating at 1.5-μm wavelength.

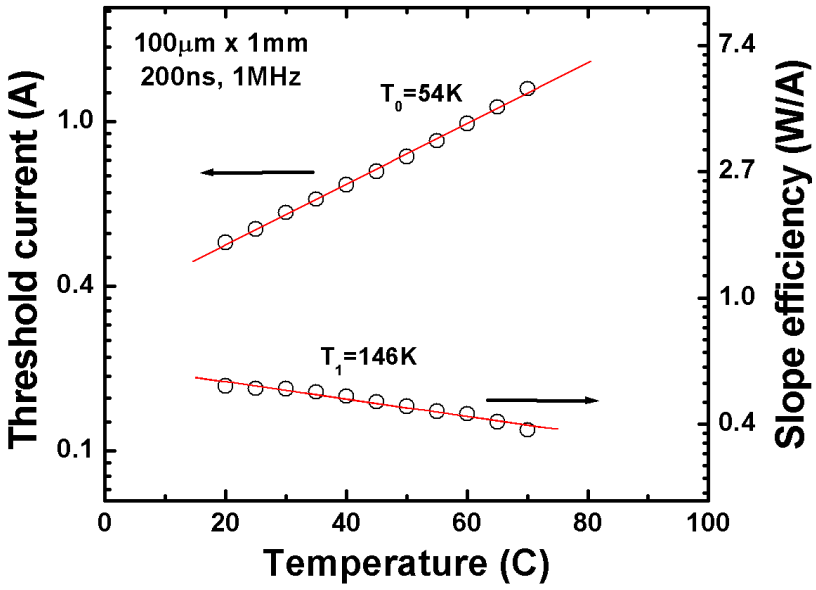

FIG. 7: Temperature dependencies of the threshold current, and the external quantum efficiency, for 1-mm-long laser measured in the pulsed regime.

To estimate the heating of the laser active region caused by power dissipation, we measured the emission spectrum red-shift with increasing drive current using an integrating sphere and an optical spectrum analyzer. To correlate wavelength shift to temperature change, a calibration factor of 0.55 nm/K was obtained by measuring the spectral shift under low-duty cycle (LDC) (0.02%), narrow-pulse-width (200 ns) excitation at a variety of heat-sink-coolant temperatures. The contribution of factors related to current change was estimated by fixing the heat sink temperature and increasing the current in LDC pulsed-mode operation. The spectral shift of laser emission spectrum due to current under LDC pulsed-mode operation was insignificant. It was concluded that the observed red-shift under cw and q-cw operation

was caused by the heating of the active region.

Layer	Composition	Thickness (nm)
p-clad	InP:Zn	1500
Outer SCH	InGaAsP (1.13 eV)	300
Inner SCH	InGaAsP (1 eV)	30
Barrier (2)	InGaAsP (1 eV)	16
QW (3)	InGaAsP (0.8 eV) 1% of compressive strain	6
Inner SCH	InGaAsP (1 eV)	30
Outer SCH	InGaAsP (1.13 eV)	300
n-clad	InP:Se	1500

TABLE I. InGaAsP/ InP laser heterostructure.

C. Design and performance of 2.3-μm single lasers

The laser heterostructure was grown by solid source molecular-beam epitaxy on n-GaSb substrates. The schematic energy band-gap diagram of laser structure is shown on the Figure 8. An $830 - nm$-thick undoped $Al_{0.25}Ga_{0.75}As_{0.02}Sb_{0.98}$ broadened-waveguide layer including the two quantum wells (QWs) is sandwiched between two $2-\mu$m-thick $Al_{0.9}Ga_{0.1}As_{0.07}Sb_{0.93}$ cladding layers. Two 200-nm-spaced 11.5-nm-wide $In_{0.41}Ga_{0.59}As_{0.14}Sb_{0.86}$ QWs provided optical gain. The n-cladding was Te-doped to $3 * 10^{17} cm^{-3}$. The p-cladding was Be-doped to $1 * 10^{18} cm^{-3}$ over

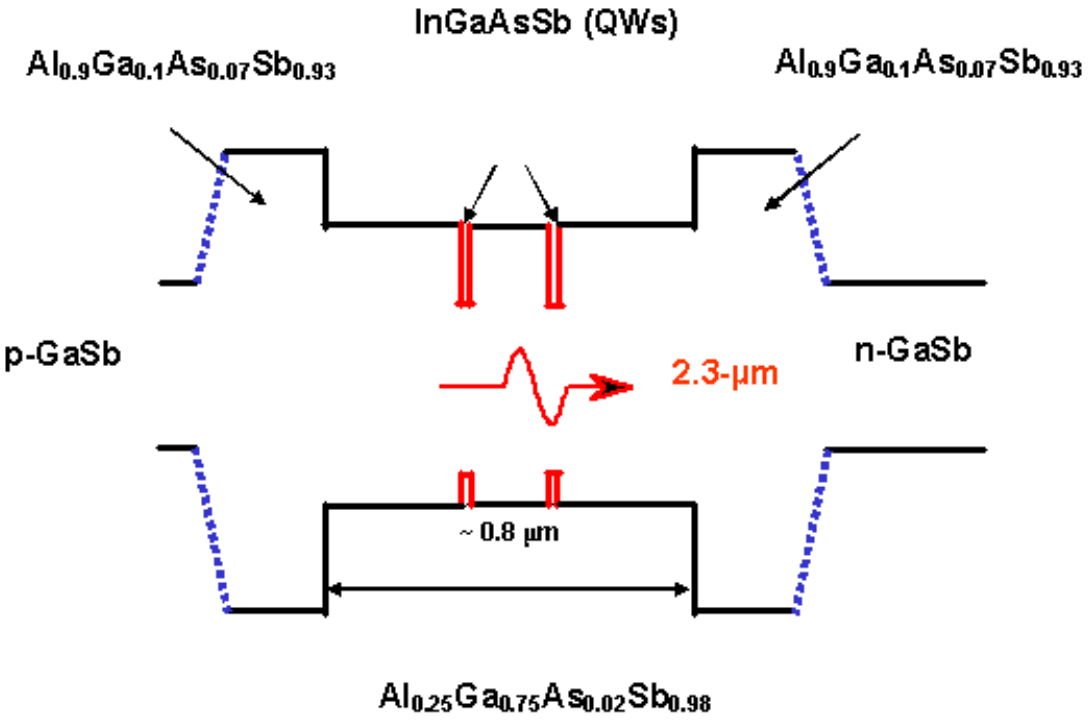

FIG. 8: Schematic energy band diagram of the broadened waveguide 2.3-μm wavelength In(Al)GaAsSb/GaSb laser.

the $0.2-\mu$m-thick layer adjacent to the waveguide, and the rest $1.8-\mu$m-thick layer was doped to $5*10^{18}cm^{-3}$ [21, 22]. This was done to reduce the internal optical loss caused by intervalance-band absorption in the p-cladding layer [40]. Heavily doped 40-nm-thick regions, compositionally graded from GaSb to $Al_{0.9}Ga_{0.1}As_{0.07}Sb_{0.93}$, have been grown between the cladding layers and the n-GaSb substrate and the p-GaSb cap layer improve electron and hole conduction. The n region is Te doped to $1*10^{18}cm^{-3}$ and the p region is Be doped to $2*10^{19}cm^{-3}$. All layers, the composition and thickness of which are given in Table II, except the QWs were grown lattice-matched to the GaSb substrate.

The wafer was processed into single emitters and was characterized. Each single

gain-guided element aperture was 100 μm defined as a window in a 0.2 μm-thick SiN dielectric layer. The facets were coated to reflect 3% and 95%. Single lasers were indium-soldered epi-side down onto copper heat sinks.

Figure 9 shows CW light-current characteristics and wall-plug efficiency for a 1-mm-long single 2.3-μm laser, taken at a heat sink temperature of 16 C. The output power was recorded by a 50-mm-diameter thermopile detector. The CW near threshold slope efficiency and threshold current were 0.2 W/A and 0.4 A. The output power saturated with current due to heating. Single lasers output 650-mW CW at 3.8 A. The wall-plug efficiency of 12% peaked at 1A. The output spectrum (insert in Figure 2) was centered near 2.36 μm; its full-width at half-maximum (FWHM) was about 14 nm at a current 2-A CW. The FWHM of the transverse far-field pattern is about 63^o and is current independent.

Figure 10 shows the performance of 100 μm-wide 1 mm-long single laser measured in pulse operation (200 ns, 1 MHz) at different heat sink temperatures. The pulsed laser external quantum efficiency and threshold current were 0.21 W/A and 360 mA (180 A/cm^2 per QW) at 20 ^oC. Figure 11 shows the threshold current and slope efficiency for a single laser as a function of temperature over the temperature range of $15^oC - 65^oC$. The empirical characteristic temperature T_0, which describes the exponential dependence of threshold current on temperature, is 95 K. T_1, the empirical characteristic temperature for slope efficiency, is 183 K.

Figure 12 shows the single laser laser emission spectra under both pulsed and

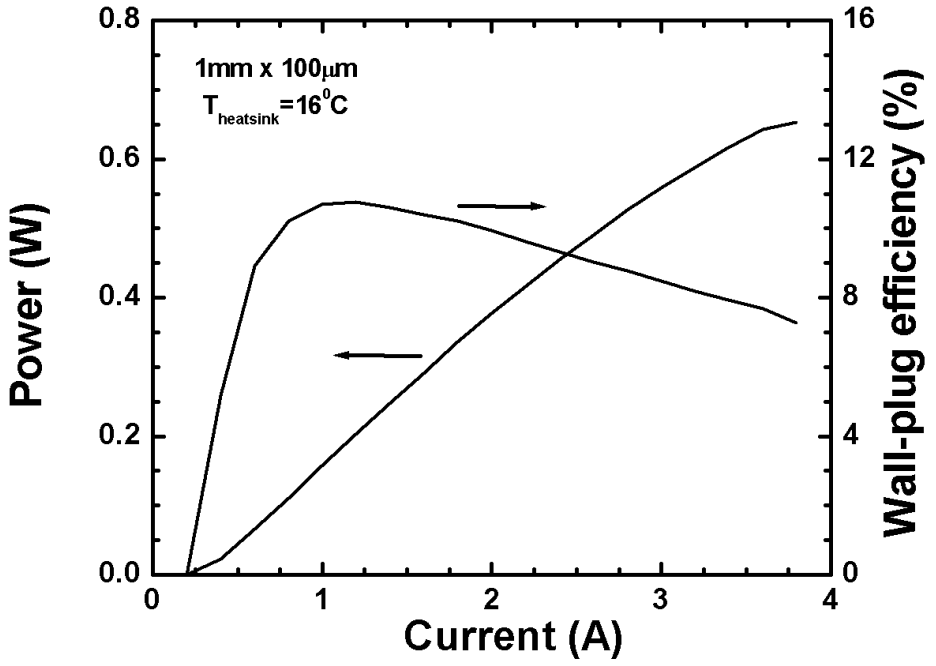

FIG. 9: Continuous-wave output-power and conversion efficiency characteristics of 2.3-μm wavelength lasers.

CW operation. To correlate wavelength shift to temperature change, we measured the spectral shift under narrow-pulse-width (200 ns) excitation at a variety of heat-sink-coolant temperatures, Figure 12a. The calibration factor of 1.2 nm/K was determined from the obtained data. The peak laser wavelength increases with temperature from about 2.33-μm at 20 C up to 2.38-μm at 60 C due to band gap reduction with increasing temperature, Figure 12b. The full-width, half-maximum (FWHM) spectral width was approximately 10 nm at a drive current of 1.5 A, broadening to 18 nm at a drive current of 3 A.

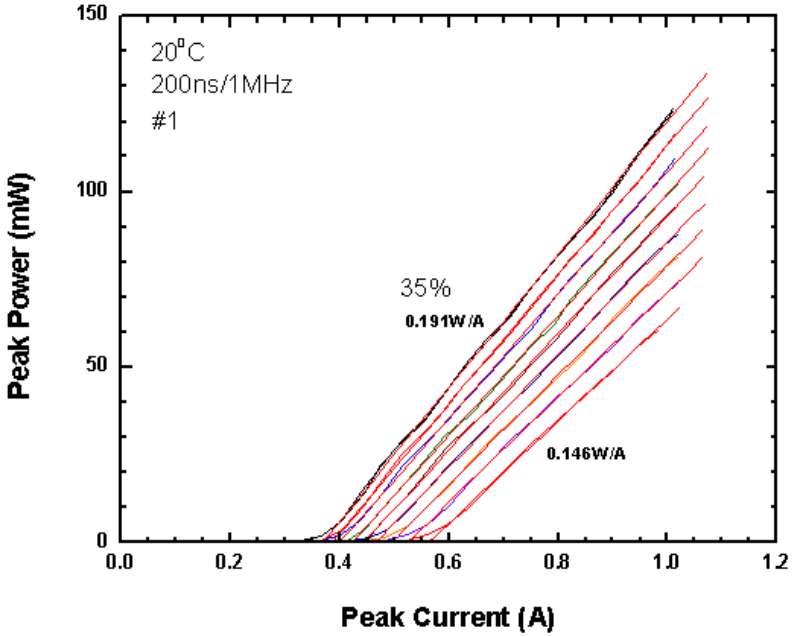

FIG. 10: Pulse mode output-power characteristics of 1 mm long and 100 μm wide single laser operating at 1.5-μm wavelength.

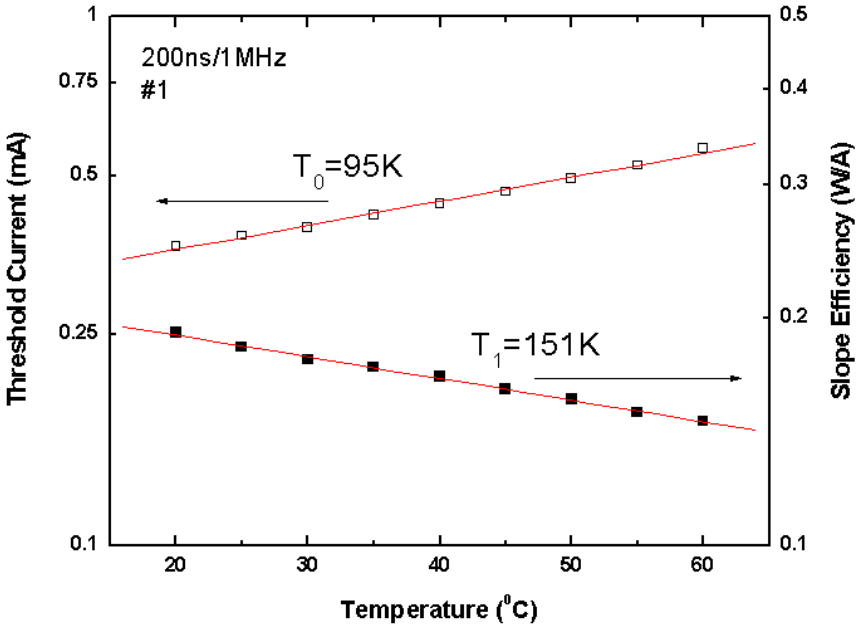

FIG. 11: Temperature dependencies of the threshold current, and the external quantum efficiency, for 1-mm-long laser measured in the pulsed regime.

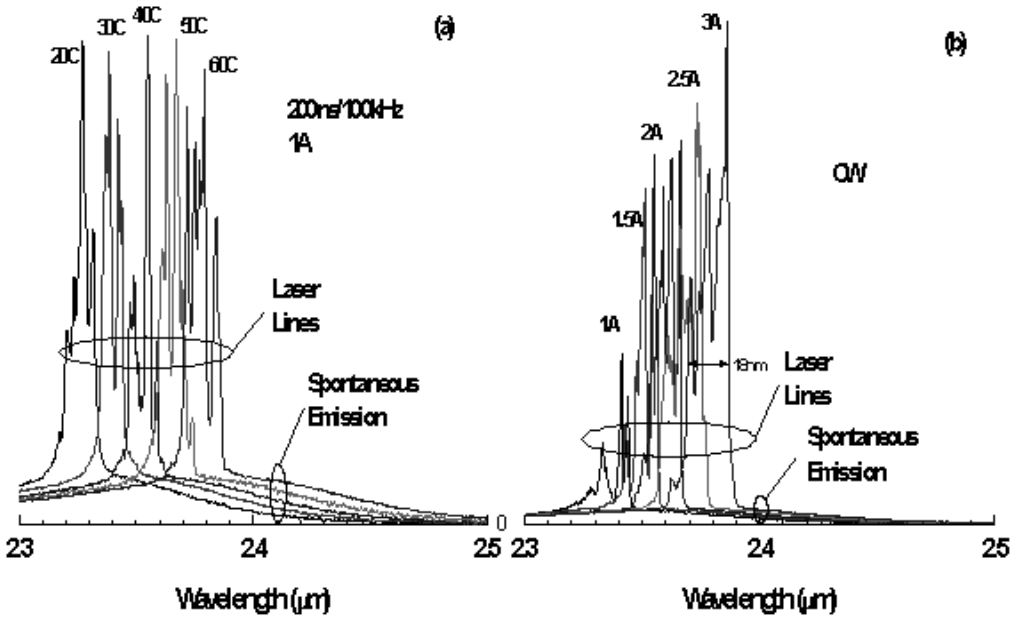

FIG. 12: Laser spectra of 2.3-μm wavelength lasers measured at several temperatures in pulsed (left) and CW (right) operation.

Layer	Thickness	Doping
cap p-GaSb	50nm	Be: $2 * 10^{19} cm^{-3}$
p-grading	40nm	Be: $2 * 10^{19} cm^{-3}$
p-clad $Al_{0.9}Ga_{0.1}As_{0.07}Sb_{0.93}$	1.8 μm	Be: $5 * 10^{18} cm^{-3}$
p-clad $Al_{0.9}Ga_{0.1}As_{0.07}Sb_{0.93}$	200nm	Be: $10^{18} cm^{-3}$
guide $Al_{0.25}Ga_{0.75}As_{0.02}Sb_{0.98}$	300nm	undoped
QW 2 $In_{0.41}Ga_{0.59}As_{0.14}Sb_{0.86}$	11.5nm	undoped
guide $Al_{0.25}Ga_{0.75}As_{0.02}Sb_{0.98}$	200nm	undoped
QW 1 $In_{0.41}Ga_{0.59}As_{0.14}Sb_{0.86}$	11.5nm	undoped
guide $Al_{0.25}Ga_{0.75}As_{0.02}Sb_{0.98}$	300nm	undoped
n-clad $Al_{0.9}Ga_{0.1}As_{0.07}Sb_{0.93}$	2μm	Te: $3 * 10^{17} cm^{-3}$
n-grading	40nm	Te: $10^{18} cm^{-3}$
buffer n-GaSb	500nm	Te:$10^{18} cm^{-3}$
substrate n-GaSb	140μm	Te: $5 * 10^{17} cm^{-3}$

TABLE II. In(Al)GaAsSb/ GaSb laser heterostructure.

D. Conclusion

In this chapter

- We present the heterostructure designs of laser diodes lasing at 1.5-μm and 2.3-μm.
- The laser diodes operating at 1.5-μm output up to 2.2 W in cw mode. The peak wall-plug efficiency was 30%.
- The GaSb-based laser diode demonstrated a cw output power of 0.65 W at 2.3-μm wavelength. The conversion efficiency peaked at 9%.

III. THERMAL RESISTANCE AND OPTIMAL FILL FACTOR OF A HIGH POWER DIODE LASER BAR

A. Introduction

A growing demand for high power optical sources led to a race to improve device reliability and increase output power. Technological development produced a gradual increase of single laser output power, however, a significant improvement took place with the fabrication of laser bars. The laser bar contains numerous individual laser emitters arranged side-by-side to form a single monolithic array. A typical laser bar might contain twenty 100 μm wide emitters equally spaced to span a 1 cm wide bar. The fill factor for such an array is defined to be the ratio of pumped bar area to total bar area.

Two solutions are most evident for increasing the laser bar output power: one is to increase the current per emitter, and the other is to increase the number of emitters. Increasing the number of fixed-width emitters on a fixed-width bar is equivalent to reducing the distance between individual emitters (i.e. increasing the fill factor). Both solutions, however, encounter an overheating problem. An increased pumping current leads not only to an increased output power but also, due to limited efficiency, to an increased dissipated power. As a result, the temperature in the active region grows which reduces the carrier confinement and increases the rate of non-radiative recombination processes. This causes an efficiency reduction so that eventually the output power saturating with increased pumping current (thermal rollover) [45].

Reducing the distance between emitters operating at constant dissipated power results in a similar heating problem. Decreasing the separation between adjacent emitters in a laser bar causes mutual heating which also leads to an active region temperature rise and decreased efficiency [11, 12]. A natural step is to reduce the distance between the emitters while also varying the pumping current in such a way that the total output power would increase. That is, we come to the problem of the optimal fill factor: finding the fill factor that allows for maximal laser bar output power.

Practically, however, laser bars are not normally operated in the regime of maximal output power. The laser temperature in this regime is quite high which reduces the device lifetime. The reliability issue leads to other approaches to the optimization problem: optimization of the distance between emitters to produce 1) maximal output power for a given active region temperature rise or 2) minimal active region temperature rise for a given output power.

Basically, all these approaches are related to the general problem of the optimization of the laser bar design. The search for the optimal fill factor when all other elements of the laser geometry (e.g., the width of the contact stripes) are fixed is an approach that allows an exact mathematical solution.

The calculation of the optimal fill factor is based on the standard phenomenological equations that describe the operation of a laser bar [45–47]. Some of the main parameters in these equations, namely, the thermal resistance characterizing the cooling rate and the series resistance characterizing the power dissipated away from the active region, depend on the fill factor. The dependence is controlled by

the laser design. The analytical expressions for the thermal and electrical series resistance for typical laser bar designs are determined, and then these expressions are used to find the optimal fill factor for a given laser bar architecture.

The central point in the evaluation of the electric resistance is the current spread calculation. In some previous publications the current density was calculated under the assumption of constant density at the contact stripe which then falls off as the square of the distance away from the contact [48–54]. An exact analytical solution to the Laplace equation that controls the current spread when carrier diffusion can be neglected was obtained by Lengyel et al. [55]. They studied a narrow stripe geometry where the width of the stripe is of the order of its distance from the active region. Similar models have been considered by Wilt [56], Joyce [57], and Agrawal [58]. A comprehensive comparison of these models has been made by Papannareddy at al. [59]. The geometry considered by Lengyel et al. [55] corresponded to the situation in ridge lasers. In high power lasers the width of the stripe is much larger than the cladding thickness, and the n-layer thickness is comparable to the stripe width. Previously, it has been shown that such a relation leads to a high current density near the edges of the active region [60].

The thermal resistance substantially depends on the thermal conductivity and geometry of the heat spreader located between the laser and the heat sink [61, 62]. Determining the thermal resistance requires the solution of the thermal conductance equation with non-trivial boundary conditions. For this purpose, a finite element method is typically used [13, 63]. However, the analytical approach allows one to understand the qualitative dependence of device characteristics on different param-

eters without performing time consuming numerical calculation required in finite element methods.

The calculated electrical series resistance is weakly dependent on fill factor. In contrast, the dependence of the thermal resistance on the fill factor is substantial. The expression obtained for the thermal resistance gives an excellent agreement with measured values without any adjustable parameters [43]. Analytical results for both resistances facilitate the calculation of the optimal fill factor.

The chapter is organized as follows. The fill factor optimization problem is formulated for a laser bar in Section III B. In sections III C and III D we present analytical solutions to the electrical and thermal problems and calculate the electric and thermal resistances. In Sec. III E we compare the theoretical and experimental values of the thermal resistance and present the theoretical results of the bar optimization.

B. Optimal fill factor

We consider a laser bar with N contact stripes with a distance a_1 between their centers, Figure 13a. The laser bar is mounted on a heat spreader which conducts heat from the laser bar to the heat sink. The heat sink is assumed ideal, i.e., its temperature is fixed and does not depend on the power dissipated in the bar. We assume that the cooling conditions for all lasers in the bar are the same and we can neglect the edge effects. In other words, the difference between the cooling of the lasers close to the ends of the bar and those in the middle can be neglected and the temperature of their active regions is the same. Indeed, we did not detect any temperature difference between different lasers in a 25 W 1.47 μm laser array that

contained 20 elements [43] (compare with Ref. [11, 12]).

If j_{th} is the threshold current in one emitter and $j > j_{th}$ is the pumping current then the optical power generated in this emitter is

$$p_{opt} = \eta(j - j_{th}) \tag{3.1}$$

where η is the differential efficiency. Well above the threshold the voltage drop across the active region, U_0 does not depend on the current and the power dissipated in one laser is

$$p_d = U_0 j + r j^2 - p_{opt} \ , \tag{3.2}$$

where r is the series resistance of one laser.

To make the result more general and avoid specifying the number of emitters (N) in a bar and the length of the bar it is convenient to deal with power dissipated per unit length of the bar, Np_d/L_b, where L_b is the length of the bar. The temperature of the active region is connected to the power dissipated per unit length by the relation $T = R_T(Np_d/L_b)$ where R_T is the thermal resistance of the unit length of the bar. At this stage it is convenient to introduce the fill factor that is defined as

$$f = \frac{Na}{L_b} \tag{3.3}$$

where a is the width of the stripe. Then with the help of Eqs.(3.1) and (3.2) the active region temperature can be expressed as

$$T = \frac{f R_T}{a} \ [\eta j_{th} + (U_0 - \eta) j + r j^2] \ . \tag{3.4}$$

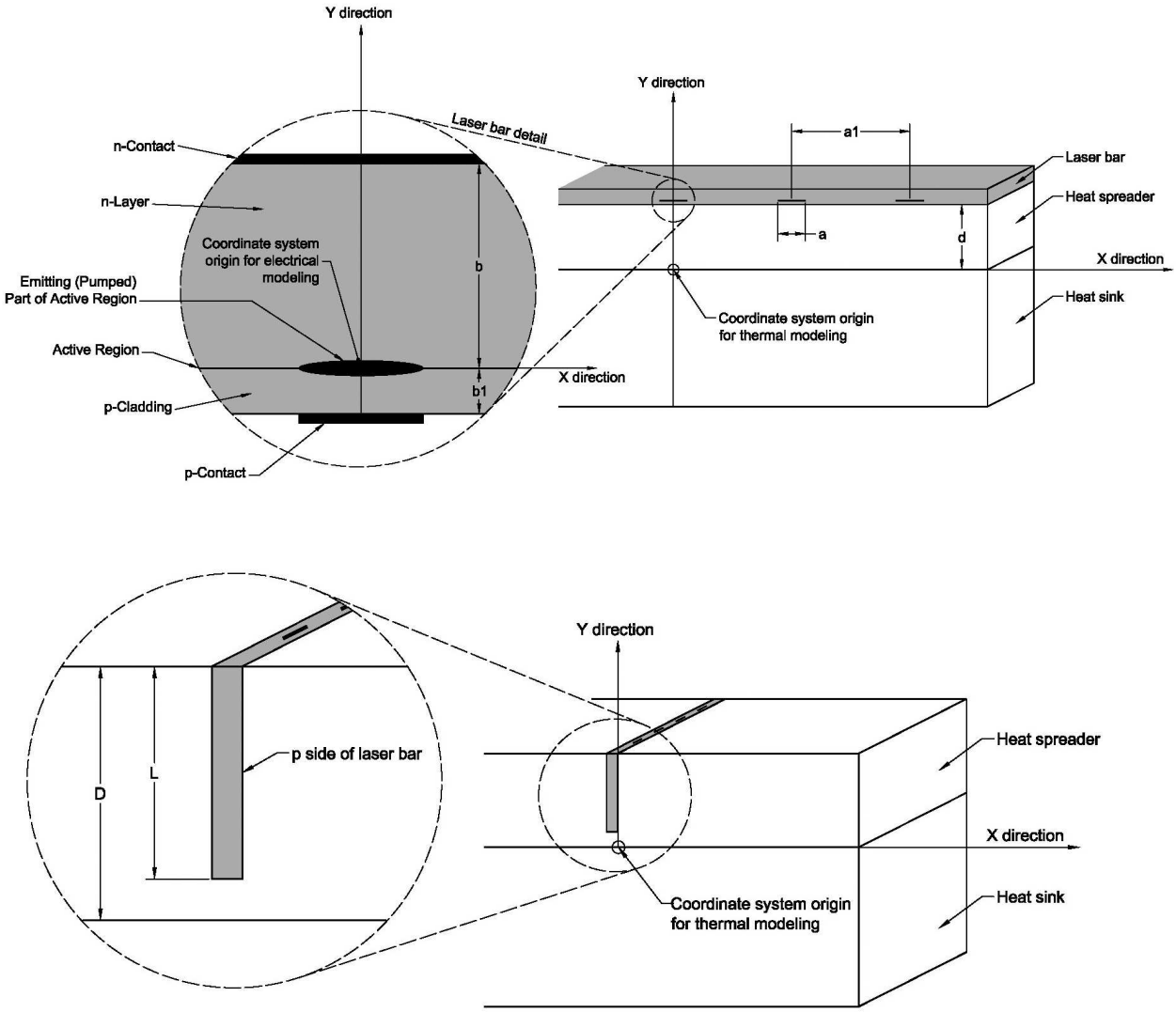

FIG. 13: Perspective views of the mounted laser bar. (a) The planar model with the laser bar, heat spreader and heat sink describing parallel planes. Light is emitted from the electrically pumped active regions defined by the multiple p-contacts of width a. The center-to-center distance between p-contacts is a_1, and the thickness of the heat spreader is d. A detailed view of the laser bar is shown in the circular inset. The inset shows that the laser bar consists of an n-layer (n-cladding and substrate) of thickness b, a thin active region and a p-clad of thickness b_1. Different coordinate systems have been used. The electrical resistance modeling employs the coordinate origin shown in the inset, the thermal resistance modeling employs the coordinate origin shown in the main drawing. (b) The perpendicular model with a similar laser bar mounted in a grooved heat spreader. The laser bar cavity length L and heat spreader thickness D are shown in the inset. The asymmetry of the n and p layer thicknesses means that the heat transfer is through the p-side of the bar which is modeled as a planar heat source of negligible thickness.

The optical power per unit length of the bar, $P_{opt} = Np_{opt}/L_b$, with the help of Eq.(3.1) can be written as

$$P_{opt} = \frac{f\eta}{a}\,(j - j_{th})\ . \tag{3.5}$$

The definition of P_{opt} and T by Eqs.(3.4) and (3.5) is not complete for two reasons. The first is that j_{th} and η depend on T. With good accuracy this dependence is usually described as

$$j_{th} = j_r e^{(T-T_r)/T_0}\ , \tag{3.6a}$$

$$\eta = \eta_r e^{-(T-T_r)/T_1}\ , \tag{3.6b}$$

where T_r is the reference temperature and constants j_r, η_r, T_0, and T_1 depend on the details of the laser structure.

The second reason is more serious and presents the main technical difficulty for the calculation of the optimal fill factor. Namely, both the thermal resistance and the series resistance depend on the fill factor. This dependence is controlled by the geometry of the laser structure and the heat spreader. The calculation of $R_T(f)$ and $r(f)$ is the main content of the chapter.

Equations (3.4) and (3.5) with known $j_{th}(T)$, $\eta(T)$, $R_T(f)$, and $r(f)$ make up the basis for the optimization problems described above, and these problems can be formulated as

- Given T, find maximal P_{opt} .
- Given P_{opt}, find minimal T .

It is necessary to note that mathematically the two problems are equivalent. Given $P_{opt}(j, T, f)$ and $T(j, f)$, both of them are reduced to the solution of the

equation

$$\frac{\partial P_{opt}}{\partial f}\,\frac{\partial T}{\partial j} - \frac{\partial P_{opt}}{\partial j}\,\frac{\partial T}{\partial f} = 0\ . \tag{3.7}$$

together with one of Eqs.(3.4) and (3.5). The equivalence can be seen from the results, Figures 15 and 16, where the plots $P_{opt}(T)$ and $T(P_{opt})$ can be obtained from each other by the transposition of the axes.

In the next two sections we present the calculation of $R_T(f)$ and $r(f)$ for simple but practically important models. For both cases we succeeded in obtaining analytical results that are quite flexible and convenient for practical applications.

C. Electric resistance of the bar

The model of the laser structure used for calculating the electric resistance is shown in Figure 13a. It consists of a p-cladding and n-layer (n-cladding with a substrate) separated by a thin region containing the waveguide and quantum wells.[62] The thickness of this quantum well region is typically smaller than 1 μm and we consider it as an interface. The n-side of the bar is uniformly covered by a metal n-contact, the p-side of the bar has multiple p-contact stripes of width a and center-to-center separation a_1. The thickness of the p-cladding b_1 is much smaller than the thickness of the n-layer b and the stripe width a. Previously, we considered a similar structure with one stripe.[60] In the system with many stripes current spreads from adjacent stripes limit each other and as a result, the resistance of the structure decreases with increasing distance between the stripes. We consider a bar with a large number of stripes so that the difference of the current spread around two stripes at

the edges of the bar can be neglected. Then it is possible to consider a periodical system of stripes with period a_1 and fill factor $f = a/a_1$.

Due to the small thickness of the p-cladding, the current spread in it can be neglected and the width of the pumped active region is the same as the stripe width. If the current density components in the p-cladding are $j_x = 0$, $j_y(x, y) = j_y(x, 0)$ and the potential at the contact stripe, U, is constant then the potential at the n-side of the active region is

$$U_a(x) = U - \sigma_p j_y(x, 0) - U_0 \ , \tag{3.8}$$

where σ_p is the conductivity of the p-cladding and U_0 is the potential drop across the active region which is assumed constant above threshold.

The current spread problem for the n-layer now can be solved independently of the p-cladding. Due to high doping in the n-layer the screening radius there is very small which makes the diffusion current negligible compared to the drift current. As a result, the potential distribution in the n-layer $\phi(x, y)$ is controlled by the Laplace equation. One of the boundary conditions for this equation is a constant potential at the n-contact, $y = b$. At the pn interface the potential is $U_a(x)$ which can be considered given only in the pumped regions while between the pumped regions the current normal to the interface is zero. The solution to this problem allows one to find $j_y(x, 0)$ as a functional of $U_a(x)$. The substitution of this functional in Eq.(3.8) provides an equation for $U_a(x)$. The solution to this equation gives the final result. In Sec. III C 1 the potential distribution in the n-layer is found analytically, in Sec. III C 2 the potential $U_a(x)$ is found with the help of a variational method, and in

Sec. III C 3 the resistance of the structure is calculated.

1. Potential distribution in n-layer

The boundary problem for the Laplace equation in the n-layer formulated above is equivalent to the boundary problem for the complex potential,

$$\chi(z) = \phi(x, y) + i\psi(x, y) \ , \tag{3.9}$$

where $z = x+iy$. Apparently, $\chi(z+a_1) = \chi(z)$ and it is enough to consider the period $|x| < a_1/2$. The system is symmetric with respect the lines $x = \pm a_1/2$ in the middle between the stripes, and the current normal to this line is zero, $\sigma_n[\partial\phi/\partial x]_{x=\pm a_1/2} = 0$ (σ_n is the conductivity of the n-layer). Then due to Cauchy-Riemann relations,

$$\frac{\partial\phi}{\partial x} = \frac{\partial\psi}{\partial y} \ , \qquad \frac{\partial\psi}{\partial x} = -\frac{\partial\phi}{\partial y} \ , \tag{3.10}$$

the boundary conditions can be written as

$$\phi = U_a(x) \ , \qquad -\frac{a}{2} < x < \frac{a}{2} \ , \ y = 0 \ , \tag{3.11a}$$

$$\psi = \text{const.} \ , \qquad \frac{a}{2} < |x| < \frac{a_1}{2} \ , \ y = 0 \ , \tag{3.11b}$$

$$\psi = \text{const.} \ , \qquad x = \pm\frac{a_1}{2} \ , \tag{3.11c}$$

$$\phi = 0 \ , \qquad y = b \ . \tag{3.11d}$$

To solve this problem it is convenient to map it first to the upper half plane of another complex variable $w = u + iv$. This can be done with the help of the transformation (see, e.g., Ref. [64, 65])

$$z = CF(\arcsin w; k) \ , \tag{3.12}$$

where $F(\theta;k)$ is the elliptic integral of the first kind. Constants C and $k<1$ are defined by the condition that point $z=a_1/2$ is mapped onto $w=1$ and point $z=a_1/2+ib$ is mapped onto $w=1/k$,

$$a_1 = 2C\boldsymbol{K}(k)\ , \tag{3.13a}$$

$$b = C\boldsymbol{K}(k')\ . \tag{3.13b}$$

where $\boldsymbol{K}(k)=F(\pi/2;k)$ is the complete elliptic integral of the first kind and $k'=\sqrt{1-k^2}$. When $w\to\infty$ Eq.(3.12) gives $z=ib$. The transformation inverse to Eq.(3.12) is expressed in elliptic sinus,

$$w = \mathrm{sn}(z;k)\ . \tag{3.14}$$

Now it is necessary to find the function $\chi(w)=\phi(u,v)+i\psi(u,v)$ analytic at the upper half plane of w and satisfying the following boundary conditions at $v=0$:

$$\phi = (U-U_0)\Phi(u)\ , \qquad -u_a<u<u_a\ , \tag{3.15a}$$

$$\psi = \text{const.}\ , \qquad u_a<|u|<1/k\ , \tag{3.15b}$$

$$\phi = 0\ , \qquad |u|>1/k\ . \tag{3.15c}$$

where

$$u_a = \mathrm{sn}(a/2C;k)<1\ , \tag{3.16}$$

$$\Phi(u) = \frac{1}{U-U_0}\,U_a[CF(\arcsin u;k)]\ . \tag{3.17}$$

The solution to this problem can be found with the help of the Keldysh - Sedov method Ref. [65, 66] and is [60]

$$\chi(w) = \frac{U-U_0}{\pi}\,[-f(w)+\psi_0 g(w)]\ , \tag{3.18}$$

where

$$f(w) \;=\; 2w\sqrt{(1-k^2w^2)(w^2-u_a^2)}\int_0^{u_a}\frac{\Phi(t)}{\sqrt{(1-k^2t^2)(u_a^2-t^2)}}\;\frac{dt}{t^2-w^2}\;, \tag{3.19a}$$

$$g(w) \;=\; 2w\sqrt{(1-k^2w^2)(w^2-u_a^2)}\int_{u_a}^{1/k}\frac{1}{\sqrt{(1-k^2t^2)(t^2-u_a^2)}}\;\frac{dt}{t^2-w^2} \tag{3.19b}$$

Here $\sqrt{1-k^2w^2}$ is defined on the plane of w with the cuts along the real axis from $w=1/k$ to ∞ and from $w=-1/k$ to $-\infty$, and is positive at the real axis between the points $-1/k$ and $+1/k$. $\sqrt{w^2-u_a^2}$ is defined on the plane of w with the cut along the real axis between the points $w=-u_a$ and $w=u_a$ and positive at the real axis at $u>u_a$. Thus the function $\sqrt{(1-k^2w^2)(w^2-u_a^2)}$ is real and positive at the real axis between the points u_a and $+1/k$ and changes sign when w changes sign. The integrals in both $f(w)$ and $g(w)$ are defined at the upper half-plane of w. They can be analytically continued to the lower half-plane across the part of the real axis where they are real.

Potential $\chi(w)$ is limited at $w\to\infty$ only if

$$\psi_0=\frac{1}{\boldsymbol{K}\left(\sqrt{1-k^2u_a^2}\right)}\int_0^{u_a}\frac{\Phi(t)dt}{\sqrt{(1-k^2t^2)(u_a^2-t^2)}}\;. \tag{3.20}$$

2. Potential at the active region

For the calculation of $j_y(x,0)$ it is convenient to introduce

$$j(z)=j_x(x,y)-ij_y(x,y)=-\sigma_n\left(\frac{\partial\phi}{\partial x}-i\;\frac{\partial\phi}{\partial y}\right)=-\sigma_n\;\frac{d\chi}{dz}\;. \tag{3.21}$$

In new variables according to Eq.(3.12)

$$j(w)=-\frac{\sigma_n}{C}\;\sqrt{(1-w^2)(1-k^2w^2)}\;\frac{d\chi}{dw}\;. \tag{3.22}$$

After the calculation of complex potential derivative this is reduced to the form

$$j(w) = \frac{2\sigma_n(U-U_0)}{\pi C \boldsymbol{K}\left(\sqrt{1-k^2u_a^2}\right)} \sqrt{\frac{1-w^2}{w^2-u_a^2}} \left[J_1(u_a,k) - J_2(w,u_a,k)\right]. \tag{3.23}$$

where

$$\begin{aligned} J_1(u_a,k) &= \boldsymbol{E}\left(\sqrt{1-k^2u_a^2}\right) \int_0^{\pi/2} \frac{\Phi(u_a\sin\theta)\ d\theta}{\sqrt{1-k^2u_a^2\sin^2\theta}} \\ &- \boldsymbol{K}\left(\sqrt{1-k^2u_a^2}\right) k^2u_a^2 \int_0^{\pi/2} \frac{\Phi(u_a\sin\theta)\sin^2\theta\ d\theta}{\sqrt{1-k^2u_a^2\sin^2\theta}}\ . \end{aligned} \tag{3.24a}$$

$$J_2(w,u_a,k) = \boldsymbol{K}\left(\sqrt{1-k^2u_a^2}\right) \int_0^{u_a} \Phi'(t)t\ \frac{\sqrt{(1-k^2t^2)(u_a^2-t^2)}}{t^2-w^2}\ dt\ , \tag{3.24b}$$

and $\boldsymbol{E}(k)$ is the complete elliptic integral of the second kind.

The substitution of $j_y(u,0)$ from Eq.(3.23) in Eq.(3.8) leads to the equation

$$\Phi(u) = 1 - \frac{b_1\sigma_n}{b\sigma_p}\ \frac{2\boldsymbol{K}(k')}{\pi} \sqrt{\frac{1-u^2}{u_a^2-u^2}}\ J_3(u_a,k)\ , \tag{3.25}$$

where

$$J_3(u_a,k) = \frac{J_1(u_a,k)}{\boldsymbol{K}\left(\sqrt{1-k^2u_a^2}\right)} - \text{V.p.} \int_0^{u_a} \Phi'(t)t\ \frac{\sqrt{(1-k^2t^2)(u_a^2-t^2)}}{t^2-u^2}\ dt\ . \tag{3.26}$$

Integral equation (3.25) determines $\Phi(u)$. The solution to Eq.(3.25) gives a minimum to the functional

$$F[\Phi] = \int_0^{u_a} \left[1 - \Phi(u) - \frac{b_1\sigma_n}{b\sigma_p}\ \frac{2\boldsymbol{K}(k')}{\pi} \sqrt{\frac{1-u^2}{u_a^2-u^2}}\ J_3(u_a,k)\right]^2 du\ . \tag{3.27}$$

This functional can be used to find an approximate solution with the help of the variational method. A good approximation is $\Phi(u) = c_1 - c_2u^2 - c_3u^8$.

3. Calculation of the resistance

The current across the n-layer is

$$I \;=\; L\int_{-a/2}^{a/2} j_y(x,0)dx = 2L\sigma_n\psi(a/2,0) = 2L\sigma_n\psi(u_a,0)\;, \tag{3.28}$$

where L is the length of the stripe. With the help of Eq.(3.18) it is possible to show that

$$\chi(u_a) = (U-U_0)\;[\Phi(u_a)+i\psi_0]\;, \tag{3.29}$$

and then

$$I = \frac{U-U_0}{r}\;, \qquad r = \frac{1}{2L\sigma_n\psi_0}\;. \tag{3.30}$$

The substitution of Eq.(3.20) gives

$$r(f) = \frac{\boldsymbol{K}\left(\sqrt{1-k^2u_a^2}\right)}{2L\sigma_n}\left[\int_0^{u_a}\frac{\Phi(t)dt}{\sqrt{(1-k^2t^2)(u_a^2-t^2)}}\right]^{-1}\;. \tag{3.31}$$

If the resistance of the p-cladding can be neglected, i.e., $b_1\sigma_n/b\sigma_p \ll 1$ then $\Phi(t)=1$ and

$$r = \frac{\boldsymbol{K}\left(\sqrt{1-k^2u_a^2}\right)}{2L\sigma_n\boldsymbol{K}(ku_a)}\;. \tag{3.32}$$

D. Thermal resistance

Typically the laser bar is mounted on a heat spreader and actively cooled heat sink. The thermal resistance of the laser bar crucially depends on the geometry of the heat spreader. In this section we calculate the thermal resistance for two different models. The first is the planar model where the bar is parallel to the heat sink and is separated by a heat spreader with given thickness d, Figure 13a. The

second model represents the bar imbedded in the heat spreader perpendicular to the interface between the spreader and the heat sink, Figure 13b. The arrays used to verify our model were fabricated using the perpendicular geometry [43]. In both models we assume an ideal heat sink in which temperature is maintained constant at any dissipated power.

1. Planar geometry

In this case the temperature field in the heat spreader is two-dimensional; there is no temperature gradient along the laser cavity, (Figure 13a). The temperature distribution can be found from the equation

$$\frac{\partial^2 T}{\partial x^2} + \frac{\partial^2 T}{\partial y^2} = 0 \ , \tag{3.33}$$

with boundary conditions

$$T(x,0) = 0 \ , \tag{3.34a}$$

$$\kappa \left.\frac{\partial T}{\partial y}\right|_{y=d} = \begin{cases} q \ , \ na_1 - a/2 < x < na_1 + a/2 \ , \\ 0 \ , \ (n-1)a_1 + a/2 < x < na_1 - a/2 \ . \end{cases} \tag{3.34b}$$

Here T is the temperature excess above the heat sink temperature, d is the width of the heat spreader, and κ is the thermal conductivity of the heat spreader material. The heat flux from each laser equals the power dissipated there, $q = p_d/La$. For the calculation of the thermal resistance of the unit length of the bar it is convenient to express the flux as the power dissipated per unit length:

$$q = \frac{P_d}{fL} \ . \tag{3.35}$$

Due to the periodicity of the boundary conditions the solution to Eq.(3.33) can be found with the help of Fourier expansion and the result is

$$T(x,y) = \frac{qa}{\kappa}\left[\frac{y}{a_1} + \frac{a_1}{\pi^2 a}\sum_{n=1}^{\infty}\frac{\sin(n\pi a/a_1)}{n^2}\,\frac{\sinh(2n\pi y/a_1)}{\cosh(2n\pi d/a_1)}\,\cos\frac{2n\pi x}{a_1}\right]. \qquad (3.36)$$

The temperature of the bar,

$$T(x,d) \;=\; \frac{qa}{\kappa}\left[\frac{df}{a} + \frac{1}{\pi^2 f}\sum_{n=1}^{\infty}\frac{\sin(n\pi f)}{n^2}\,\tanh\frac{2n\pi df}{a}\,\cos\frac{2n\pi x f}{a}\right], \qquad (3.37)$$

oscillates with x, i.e., along the bar. It reaches its maximum in the middle of a stripe, $x = 0$, and minimum between two stripes, $x = a_1/2$. The amplitude of the oscillations decreases with increasing fill factor and at $f = 1$ the temperature of the bar is x independent: $T(x,d)|_{f=1} = qd/\kappa$

The measured laser temperature corresponds to the temperature averaged across the laser, i.e.,

$$T_{av} \;=\; \frac{1}{a}\int_{-a/2}^{a/2} T(x,d)dx = \frac{qa}{\kappa}\left[\frac{df}{a} + \frac{1}{\pi^3 f^2}\sum_{n=1}^{\infty}\frac{\sin^2(n\pi f)}{n^3}\,\tanh\frac{2n\pi df}{a}\right] \qquad (3.38)$$

This gives the following expression for the thermal resistance of the unit length of the bar,

$$R_T = \frac{T_a}{P_d} = \frac{d}{\kappa L} + \frac{a}{\kappa\pi^3 f^3 L}\sum_{n=1}^{\infty}\frac{\sin^2 n\pi f}{n^3}\,\tanh\frac{2n\pi df}{a}\;. \qquad (3.39)$$

The thermal resistance decreases with increasing fill factor and reaches the value of $d/\kappa L$ when $f = 1$. A decreasing thermal resistance with increasing fill factor has also been obtained using the finite element method [13].

2. Perpendicular geometry

In the perpendicular geometry, Figure 13b, the temperature depends on all three coordinates: it depends on the distance from the bar, it changes along the cavity due to the varying distance to the heat sink, and it changes in the direction along the bar similarly to the planar model. The exact calculation of the three dimensional temperature field gives quite cumbersome results. However, practically it is necessary to know the temperature close to the maximal one. For the temperature close to the maximum a very good approximation can be obtained in a relatively simple way.

For this reduction, first the temperature field in the perpendicular geometry is calculated for a fill factor of 100%. Then the effective thickness of an equivalent planar geometry heat spreader is determined such that it provides the 100% fill factor bar temperature equal to the maximal temperature in the perpendicular geometry at the same 100% fill factor. After the effective thickness is chosen the bar temperature can be calculated with any fill factor with the help of Eq.(3.39). An excellent matching of this approximation to experimental results has been achieved.

The calculation of the maximal temperature in the perpendicular geometry with a fill factor of 100% is reduced to a two-dimensional problem for the Eq.(3.33) at a stripe with a cut, see Figure 13b. The boundary conditions for this equation are the following. The temperature excess equals zero at the interface with the heat sink, $y = 0$. The heat flux comes in only from the p-side of the bar, $D - L < y < D$, $x = +0$. The heat flux from the n side, $D - L < y < D$, $x = -0$, can be neglected

because of the large thickness of the substrate compared to the thickness of the p-cladding. That is

$$T(x,0) = 0 \ , \qquad \left.\frac{\partial T}{\partial y}\right|_{y=D} = 0 \ , \tag{3.40a}$$

$$\left.\frac{\partial T}{\partial x}\right|_{\substack{x=-0 \\ D-L<y<D}} = 0 \ , \qquad \kappa \left.\frac{\partial T}{\partial x}\right|_{\substack{x=+0 \\ D-L<y<D}} = -q \ , \tag{3.40b}$$

The problem can be solved with the conformal mapping of the stripe with the cut $x = 0$, $D - L < y < D$ at the plane $z = x + iy$ to the stripe $0 < v < \pi$ at the plane $w = u + iv$. The mapping is carried out with the help of the function [65]

$$w = \ln \frac{\cos\dfrac{\pi L}{2D}\sqrt{\coth^2\dfrac{\pi z}{2D} + \tan^2\dfrac{\pi L}{2D}} + 1}{\cos\dfrac{\pi L}{2D}\sqrt{\coth^2\dfrac{\pi z}{2D} + \tan^2\dfrac{\pi L}{2D}} - 1} \ . \tag{3.41}$$

The Laplace equation for T in the plane z remains the Laplace equation in the plane w. The boundary conditions at the plane w are

$$T(u,0) = 0 \ . \tag{3.42a}$$

$$\left.\frac{\partial T}{\partial v}\right|_{v=\pi} = \begin{cases} \dfrac{q}{\kappa}\ \dfrac{D}{\pi}\ \dfrac{\cos\dfrac{\pi L}{2D}\ \tanh\dfrac{u}{2}}{\sqrt{\sin^2\dfrac{\pi L}{2D} - \tanh^2\dfrac{u}{2}}} \ , & 0 < u < u_D \ , \\ 0 \ , & \text{otherwise} \ . \end{cases} \tag{3.42b}$$

The solution in the stripe $0 < v < \pi$ can be found with the help of expansion in Fourier integral in u or Fourier series in v and the result can be reduced to the form

$$T(u,v) = \frac{1}{2\pi}\ \frac{qD}{\pi\kappa}\int_0^{u_D} \ln\left[\frac{\cosh[(u-u')/2] + \sin(v/2)}{\cosh[(u-u')/2] - \sin(v/2)}\right] \frac{\cos\dfrac{\pi L}{2D}\ \tanh\dfrac{u'}{2}}{\sqrt{\sin^2\dfrac{\pi L}{2D} - \tanh^2\dfrac{u'}{2}}}\ du' \tag{3.43}$$

The temperature reaches its maximum at $y = D$, $x = +0$ or $u = u_D$, $v = \pi$ and it is

$$T_m = \frac{1}{2\pi}\ \frac{qD}{\pi\kappa}\int_0^{u_D} \ln\left[\frac{\cosh[(u_D-u)/2] + 1}{\cosh[(u_D-u)/2] - 1}\right] \frac{\cos\dfrac{\pi L}{2D}\ \tanh\dfrac{u}{2}}{\sqrt{\sin^2\dfrac{\pi L}{2D} - \tanh^2\dfrac{u}{2}}}\ du \ . \tag{3.44}$$

A comparison of this expression with the temperature in the plane geometry for $f = 100\%$, $T_m = qd/\kappa$, immediately gives the following expression for the effective thickness:

$$d \;=\; \frac{D}{2\pi^2}\int_0^{u_D} \ln\left[\frac{\cosh[(u_D-u)/2]+1}{\cosh[(u_D-u)/2]-1}\right] \frac{\cos\dfrac{\pi L}{2D}\;\tanh\dfrac{u}{2}}{\sqrt{\sin^2\dfrac{\pi L}{2D}-\tanh^2\dfrac{u}{2}}}\;du\;. \quad (3.45)$$

Now the thermal resistance can be calculated with the help of Eq.(3.39) where d is taken from Eq.(3.45).

E. Results and discussion

We compare our optimization theory with experimental results obtained on laser bars based on InGaAsP/InP and operating at 1.5-μm. In the next chapter IV B we consider the operational characteristics and design details of laser arrays. The measurements were made on bars with different fill factors, 10%, 20% and 40%. In all bars the width of the n-contact stripes was $a = 100\mu$m. The distance between the n- and p-contacts was 140 μm, the thickness of the p-cladding was $b_1 = 1.5$ μm and the conductivities of the n-layer and p-cladding were $\sigma_n = 320$ $\Omega^{-1}\text{cm}^{-1}$ and $\sigma_p = 1.6$ $\Omega^{-1}\text{cm}^{-1}$. This gives the ratio of the resistances of the p-cladding and the n-layer necessary for the calculation of the electric resistance $b_1\sigma_n/b\sigma_p = 2$ (here b_1 and σ_p are the thickness of the conductivity of the p-cladding). The details of laser heterostructure were discussed in the chapter II B.

The laser bars were mounted in metallized grooves in BeO heat spreaders which were bonded to water-cooled microchannel heat sinks, Figure 13b. The thickness of the heat spreader was $D = 1.5$ mm, and the cavity length for these bars was 1 mm. According to Sec. III D 2 the thermal resistance of the bar in this geometry is equivalent to the thermal resistance in the planar geometry, Figure 13a, with an effective thickness $d = 8.3a$ obtained from Eq.(3.45). Using $d = 830$ μm in Eq.(3.39) the thermal resistance was calculated for laser bars in the perpendicular geometry for different bar designs. These results were compared to experimentally measured thermal resistances. The measured dependence of the active region overheating vs the dissipated power density is given in Figure 14(a). The slopes of the straight

lines fitted to the experimental data in Figure 14 provide estimates of the thermal resistance for bars with different fill factors. Thermal resistances of bars with f equal 0.1, 0.2, and 0.4 are respectively 0.56, 0.40, and 0.36 K cm/W. The standard deviation of measured points from the linear fits gives the accuracy of the thermal resistance around 4% or smaller. The maximal error coming from the error of the temperature measurements is close to this value. Eq.(3.39) gives for these bars 0.58, 0.41, and 0.35 K cm/W. That is the discrepancy between the theoretical and experimental results is within the accuracy of the measurements. The thermal resistance of bars with 2 mm cavities mounted in heat spreaders of CuW were also evaluated (Figure 14(b)). For these bars, we compare the ratio of the thermal resistances for the 0.1 and 0.4 fill factor bars. The experimentally determined ratio is 1.5, close to the calculated ratio of 1.64.

Along with the calculated dependencies of $r(f)$ and $R_T(f)$, the temperature dependencies of the threshold current and slope efficiency are required to solve the optimization problem Eq.(3.7). These parameters were measured (chapter II B) under short pulse operation by changing the heat sink temperature for individual 1 mm cavity length lasers. Both the threshold current j_{th} and slope efficiency η are well described by Eq.(3.6) with $j_r = 0.5$ A, $\eta_r = 0.5$ W/A, $T_r = 20\ \ C$, $T_0 = 54\ \ K$, and $T_1 = 160\ \ K$. The voltage across the active region above threshold $U_0 = 0.91\ \ V$.

The solution of the optimization problem (Eq(3.7)) yields the maximum output power for a given active region temperature rise, as shown by the solid line in Figure 15. The dashed line in Figure 15 corresponds to the optimal fill factor design that provides this output power at the given active region temperature rise. A similar

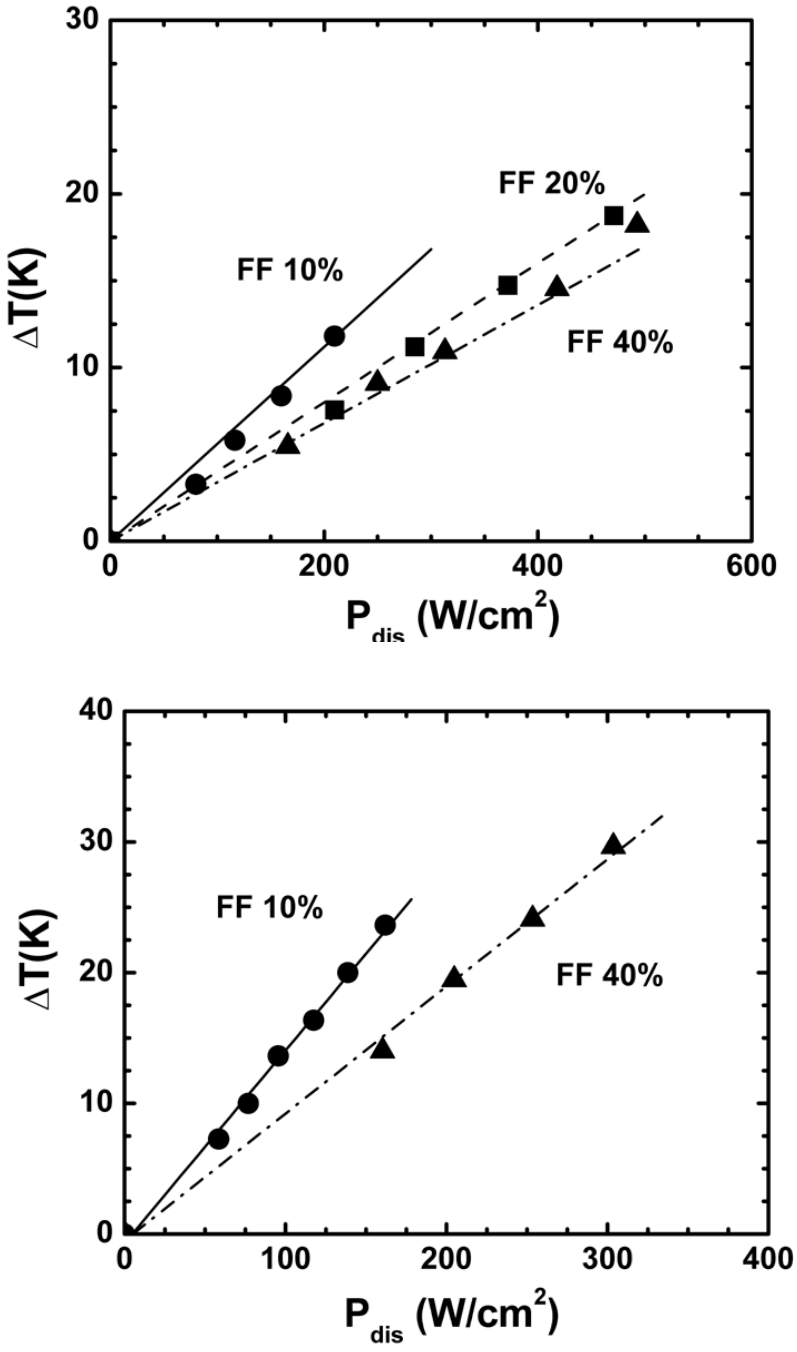

FIG. 14: Measured overheating of the active region versus dissipated power density p_{dis} (a) for different fill factor laser bars with 1 mm long cavities mounted in BeO heat spreaders and (b) for different fill factor laser bars with 2 mm long cavities mounted in CuW heat spreaders. Solid symbols indicate data points (circles, squares, and triangles for 10%, 20%, and 40% fill factors respectively). Lines fit to the experimental data are used to determine the thermal resistance.

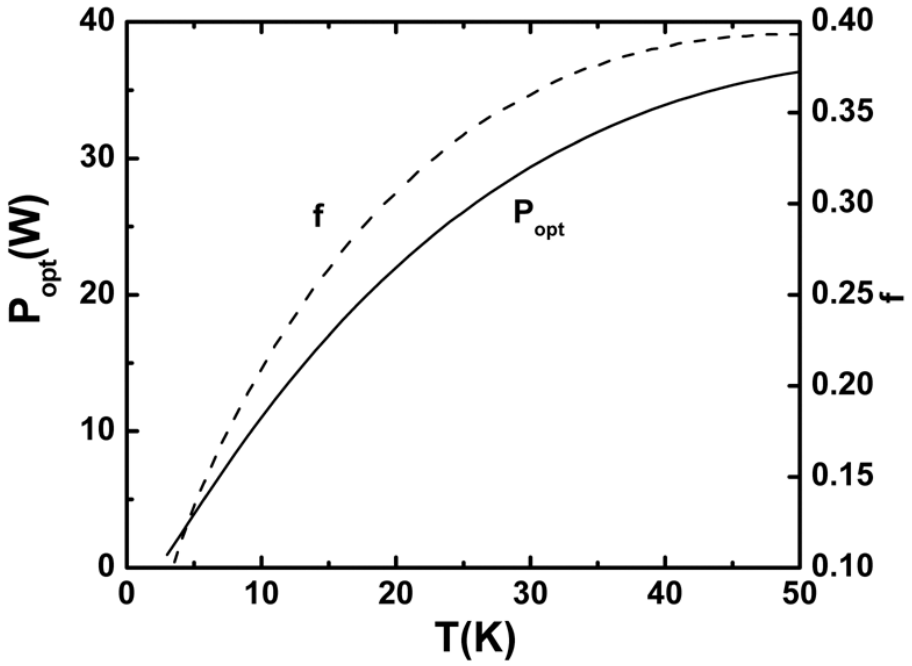

FIG. 15: Optimized fill factor (dashed line) and corresponding maximum output power (solid line) as a function of laser temperature rise.

optimization based on minimal temperature rise for a given output power is shown in Figure 16. Here again, the dashed line represents the optimal fill factor, and the solid line indicates the minimal active region temperature rise for the given output power.

To understand how critical the optimal fill factor is, we compare the analytically calculated active region temperature rise versus output power for an optimal fill factor array and for several fixed (10%, 20% and 40%) fill factor arrays. This comparison is given in Figure 16. The 40% fill factor array plot is nearly coincident with the optimal fill factor plot above about 25 W. For output powers below 17 W, the difference in active region temperature between the optimal array and the 20% fill factor array is negligible. The 10% fill factor array has the highest temperature

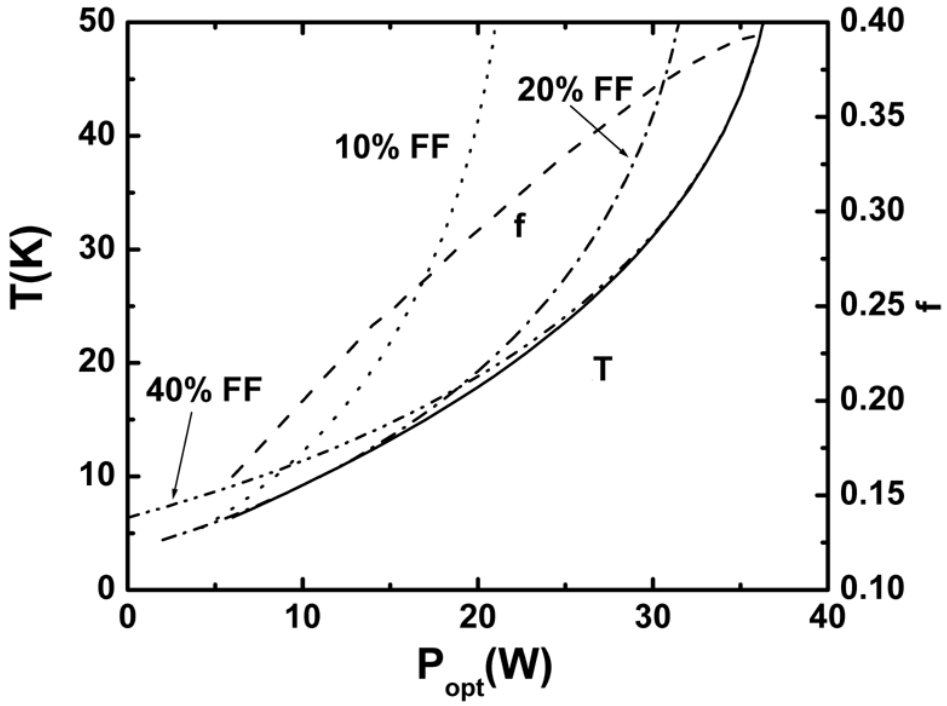

FIG. 16: Optimized fill factor (dashed line) and corresponding minimal laser temperature rise (solid line) as a function of output power. The dotted lines show the temperature rise for several fixed fill factor arrays as a function of output power.

among the rest arrays above 5W. Clearly, the optimal fill factor depends on the bar operating regime.

Earlier we suggested two methods of increasing array output power: increasing the pumping current per emitter and increasing the number of emitters. By calculating the optimal fill factor for a particular operating regime, we have found the most favorable balance between these two approaches. The optimal fill factor curve shown in Figure 15 illustrates that for increasing output power in this system, it is preferable to use a higher fill factor. Higher fill factors offer advantages for higher power operation since the effect of mutual heating is weaker than the heating of each one of them by the current.

F. Conclusion

In this chapter

- We obtained analytical expressions for the steady state electrical and thermal resistance of a laser bar. Both quantities depend on geometry, and in particular, the fill factor.

- Theoretical results for the thermal resistance are in excellent agreement with the measured thermal resistance of 1 and 2 mm cavity length laser arrays with different fill factors.

- We use the analytical results to calculate the optimal laser bar fill factor. The value of the optimal fill factor depends on the working regime of the bar; higher output powers require higher fill factors for minimum active region temperatures.

IV. PERFORMANCE OF INFRARED HIGH-POWER LASER DIODE ARRAYS

A. Introduction

Replacing flash-lamps with efficient, narrow-band diode laser pumping sources significantly increased the maximum available power and extended the application area of solid-state lasers. In recent years, there has been an increased interest in the development of high-energy, Q-switched solid-state sources operating in eye-safe wavelength range. Optically pumped erbium-doped crystalline hosts offer great potential as efficient, pulsed, eye-safe laser sources. The further progress of Er:doped solid state laser is determined by the development of high-power laser arrays reliably delivering energy in Er absorption bands near 1.5-μm. High-power electrically pumped semiconductor laser arrays operating near 2.3-μm can be used for optical pumping of recently developed type-II semiconductor lasers [37].

This chapter describes the design and performance of infrared laser diode arrays. It is organized as follow. In section IV B we consider the details of design and performance of high-power laser arrays fabricated for optical pumping of Er:YAG solid-state lasers. The operation of 2.3-μm laser arrays is discussed in section IV C. The steady-state thermal analysis of high-power laser diode arrays is considered in the section IV D.

B. Design and performance of 1.5-μm laser arrays

The laser arrays operating at 1.5-μm were fabricated from InGaAsP/InP wafer grown by organometallic chemical vapor deposition. The laser active region consisted of three 6-nm-thick compressively strained quantum wells incorporated into a two-step graded index waveguide with a total thickness of 710 nm. The laser facets were high-reflection/anti-reflection coated with reflection coefficients of 95% and 3%, respectively. Single 100-μm-wide, 1-mm-long lasers demonstrated a threshold current density of 480 A/cm^2 and a differential efficiency of 60%. Over the temperature range from 18 to 60 ^{o}C, the threshold characteristic temperature T_0 was 54 ^{o}K and the slope-efficiency characteristic temperature T_1 was 160 ^{o}K. The performance of single emitters is described in details in section II B.

Based on the characterization results of single emitter performance (chapter II B) and the solution for laser bar design optimization (chapter III), we chose the design of laser diode bar. We used 1-cm-long laser bars containing twenty 100-μm-wide emitters equally spaced over 10 mm laser bar with 500 μm center-to-center distance, yielding a fill factor of 20%. The laser cavities were 1 mm long to fit the standard heat sink assembly. One-dimensional (1D) and two-dimensional (2D) arrays were fabricated by mounting one bar or multiple bars in metallized grooves in BeO blocks (heatspreaders), which were bonded on water-cooled microchannel heat sinks. This arrangement removes heat from both sides of the laser bar.

Figure 17 shows the current dependencies of the cw and q-cw (5-ms pulse duration, 20-Hz pulse repetition frequency) output power and the wall-plug efficiency for

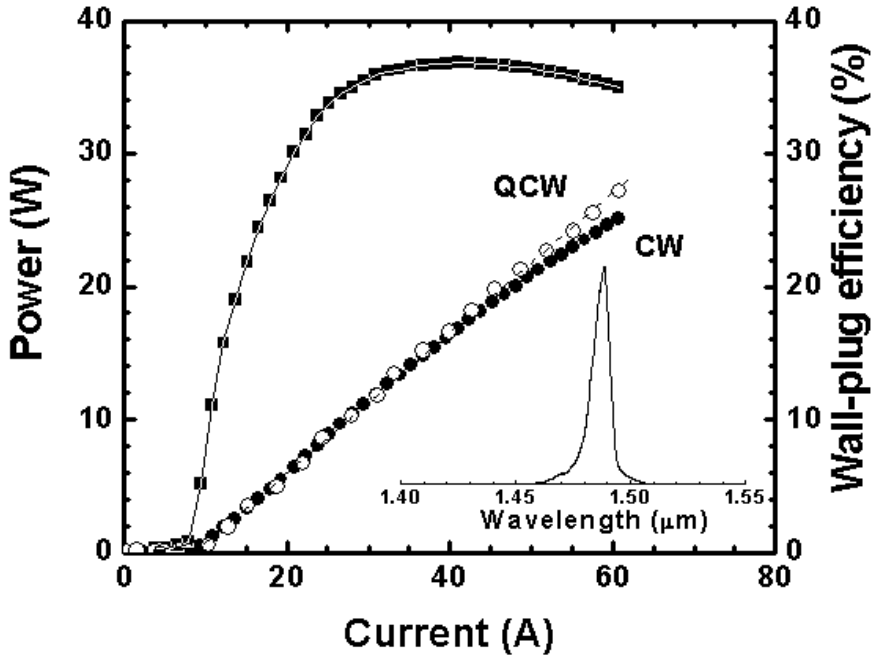

FIG. 17: Output power (circles) and wall-plug efficiency (squares) of a 1.5-μm 1-D array operated in q-CW (open symbols) and CW (closed symbols) modes at a coolant temperature of 16 ^{o}C. Inset demonstrates integrated emission spectrum of the array measured at 40 A and 18 ^{o}C.

a 1D diode array at a coolant temperature of 16 ^{o}C. The output power was recorded by a 50-mm-diameter thermopile detector. The slope efficiency of 0.5 W/A remained constant in q-cw mode up to the measured output power of 27 W. The power thermal rollover in cw mode was observed when the drive current exceeded 40 A. The maximum wall-plug efficiency was 37% at 40 A, and was better than 34% up to the maximum drive current of 60 A.

To estimate the heating of the laser active region caused by power dissipation, we measured the emission spectrum red-shift with increasing drive current. The temperature change was recalculated from wavelength shift using a calibration factor of 0.55 nm/K determined in section II B. At 60-A drive current, the active-region

temperature rise was 18 ^{o}K in the cw mode and 13 ^{o}K in the q-cw mode. The thermally induced rollover of cw output power appeared in LI-characteristics at active region temperature of 28 ^{o}C.

The inset of Figure 17 shows the integrated emission spectrum of the 1D array measured at an 18 ^{o}C coolant temperature. The full-width at half-maximum of the emission spectrum of 1D laser array was about 8 nm.

A 2D laser array consisted of series connected four bars with a bar-to-bar pitch of 3.2 mm. Each bar had twenty 100 μm wide emitters equally distributed over 1 cm laser bar. A q-cw output power of 110 W was achieved at a current of 60 A, as shown in Figure 18. The 2D array integrated emission spectra were measured at a current of 30 A in q-cw mode at 18 and at 25 ^{o}C as shown in the inset in Figure 18. The spectrum shifted with temperature, while the full width at half maximum spectral width remained at about 10 nm.

C. Design and performance of 2.3-μm laser arrays

The laser heterostructure was grown by solid source molecular-beam epitaxy on n-GaSb substrates. The device consisted of a 800-nm-thick $Al_{0.25}Ga_{0.75}As_{0.02}Sb_{0.98}$ broadened-waveguide layer consisting of two QWs sandwiched between 2-μm-thick $Al_{0.9}Ga_{0.1}As_{0.07}Sb_{0.93}$ cladding layers. The details of single laser characterization and design are discussed in the chapter II C and [21, 22, 25]. Based on the characterization of single emitter devices (chapter II C), we determined an optimal(chapter III) laser bar design for cw and qcw operations.

A 1-cm-wide 1-mm-long anti-reflection/high-reflection coated laser bar containing

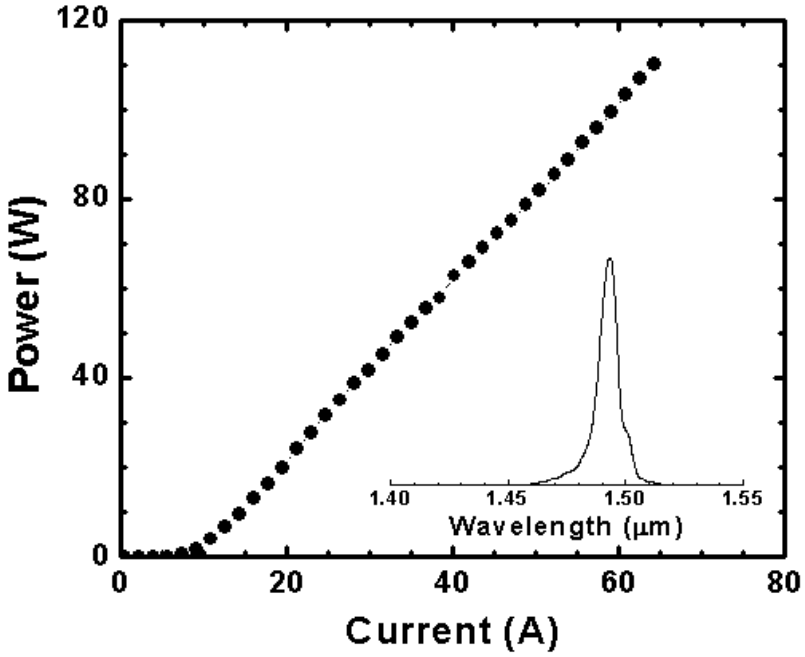

FIG. 18: Output power of a 2-D array operated in the q-cw mode at 18 ^{o}C. Inset demonstrates integrated emission spectrum of a 2-D array recorded at 40 A and 18 ^{o}C.

19 100-μm-wide emitters separated by 500 μm was soldered into a microchannel-cooled BeO heat sink. Figure 19 shows its light-current characteristics and wall-plug efficiency, as well as its spectrum (insert) at 30 A cw, all measured at 18 C. The maximum CW power of 10 W is reached at 70 A. The spectrum is centered near 2.36-μm with a FWHM of about 20 nm at 30-A cw. In the qCW mode (30 μs, 300 Hz, 0.9% duty cycle) the array output over 18.5-W peak power at a peak current of 100 A. In the short-pulse, low-duty-cycle mode, the light-current characteristics is linear up to nearly 20 W of peak power at 100 A of peak current without any cooling.

Array heating causes saturation of the cw and qcw light-current characteristics. The thermal resistance of the array with 20% fill factor is about 0.4 K/W and

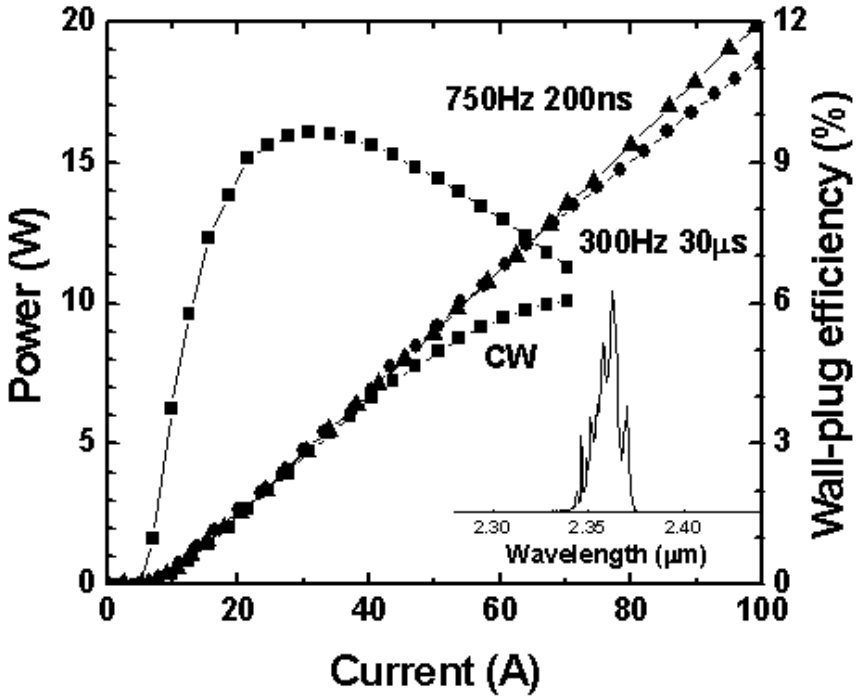

FIG. 19: Current characteristics of output-power and wall-plug efficiency of 2.3-μm laser linear array. The light-current characteristics in cw and q-cw were measured at 18 ^{o}C coolant temperature and at room temperature (uncooled) in short pulse operation. The inset shows the laser array emission spectrum measured at 30-A drive current and 18 ^{o}C coolant temperature in CW operation.

was determined from the emission spectrum red shift with power dissipation. This result is in good agreement with analytically calculated one in the chapter III D. This thermal resistance leads to active region overheating of about 25 ^{o}K at an output power of 5-W cw and about 75 ^{o}K at 10 W. The somewhat excessive heating at high currents is related to the wall-plug efficiency (9% maximum). The array cw output power could be increased substantially if the wall-plug efficiency is improved.

The relatively low laser power conversion efficiency is attributed to 1) 50% internal efficiency about 50% of the injection current after threshold is parasitic, and 2) excess voltage drop across the laser heterostructurethe voltage at threshold is about

1 V and it rises up to over 2 V at 3 A for a single laser, while laser energy quantum is only 0.54 eV.

The internal efficiency is reduced by lateral current spreading and nonradiative Shockley - Reed - Hall recombination in the waveguide layer [67, 68]. Lateral current spreading is substantial in the current laser design since no steps were taken to confine carriers laterally at the time of wafer processing [67]. Lateral current spreading can be expected in the 2-μm p-cladding and 800-nm waveguide layers as well as from lateral diffusion in the QWs [68].

The parasitic barriers for carrier transport from cladding to waveguide layer makes a large contribution to the excessive voltage drop and series resistance [69]. Careful adjustment of the cladding/waveguide material composition and doping profile can reduce the excessive voltage drop across the laser heterostructure.

Once the laser power conversion efficiency is improved, the optimum laser bar fill-factor will be higher than the current 20%, thus increasing the maximum power from a single bar.

D. Steady-state thermal analysis of high-power laser arrays

The limited wall-plug efficiency of high power laser arrays leads to a considerable amount of heat generated under high power steady state operation. To reduce array overheating, the common approach is to increase the area through which the heat is dissipated (thermal foot print). The thermal foot print can be enlarged by extending the cavity length, or increasing the number of emitters. For the array architecture of Figure 13, a cavity length increase requires thicker heat spreader blocks. The

thicker heat spreader leads to a longer heat propagation length towards the heat sink and higher thermal gradient along the cavity length [43, 70]. The electrically pumped active region area of the laser bar can be efficiently increased by reducing the distance between adjacent stripes of constant width (i.e. by increasing the fill factor). However, decreasing the separation between adjacent emitters can lead to increased mutual heating. The effect of fill factor on overheating is considered in this section.

The temperature of the active region is a critical factor in the operational lifetime of the array. Previous results indicate that the lifetime is exponentially dependent on the active region temperature [71, 72]. The main factors determining the temperature of the active region are the power dissipation in the active area, the series resistance of the cladding layers, and the mutual heating of adjacent emitters.

To study the influence of laser bar design on overheating, we fabricated InP-based arrays with fill factors of 10%, 20% and 40% and measured the dependence of the active region temperature change on dissipated power (P_{dis}), which is defined as the difference between input electrical power and output optical power. The overheating of the laser active region was obtained by measuring the emission spectrum red-shift. As can be seen in the Figure 20, the active-region temperature depends linearly on dissipated power with the thermal resistance as the coefficient of proportionality. The thermal resistances of 0.56, 0.4, and 0.34 K/W were experimentally determined for 10%, 20% and 40% fill factor arrays, respectively. The thermal resistance was found to be significantly decreased by increasing fill factor from 10% to 20% and changed much less with further fill factor increases. The inset shows this decreasing

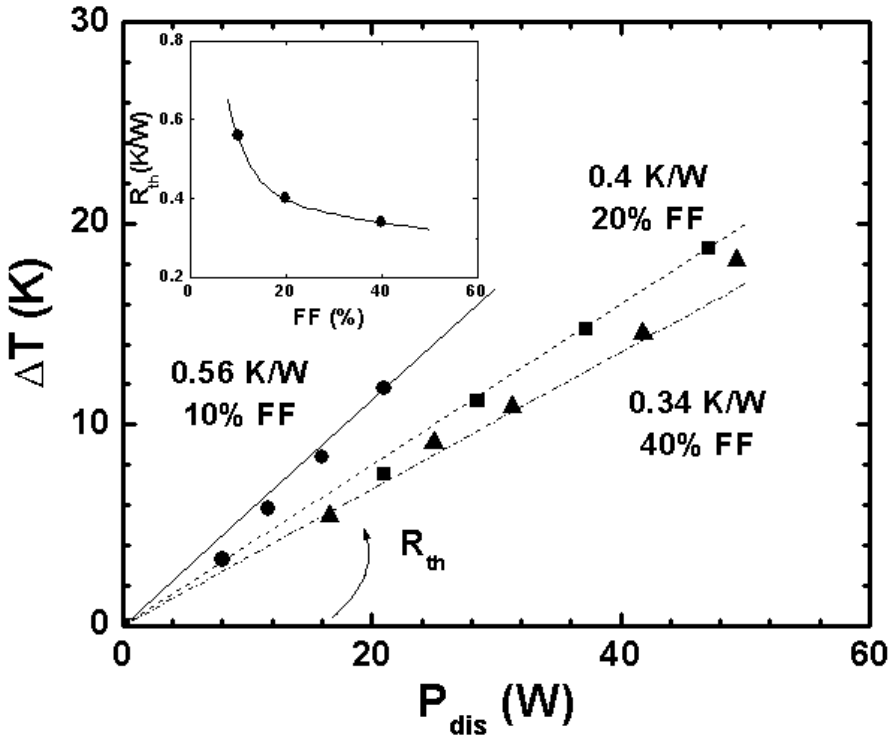

FIG. 20: The experimentally measured active-region temperature rise as a function of dissipated power is shown for different fill factor arrays. The inset shows the dependence of the thermal resistance on fill factor.

dependence of thermal resistance on fill factor, which saturates at high FF, in good agreement with Ref. [73].

This dependence of the thermal resistance on the fill factor results from a nonuniform temperature distribution in the laser bar. To clarify the experimental results, we developed an analytical model (chapter III D) based on the solution of the heat conduction equation with non-trivial boundary conditions defined by the geometry of laser array. In this thermal model, we simulated the real geometry (Figure 13b) with a structure in which the laser bar, the BeO layer, and the ideal heat sink are coplanar (Figure 13a). The 830-mm thickness of the BeO layer was determined by

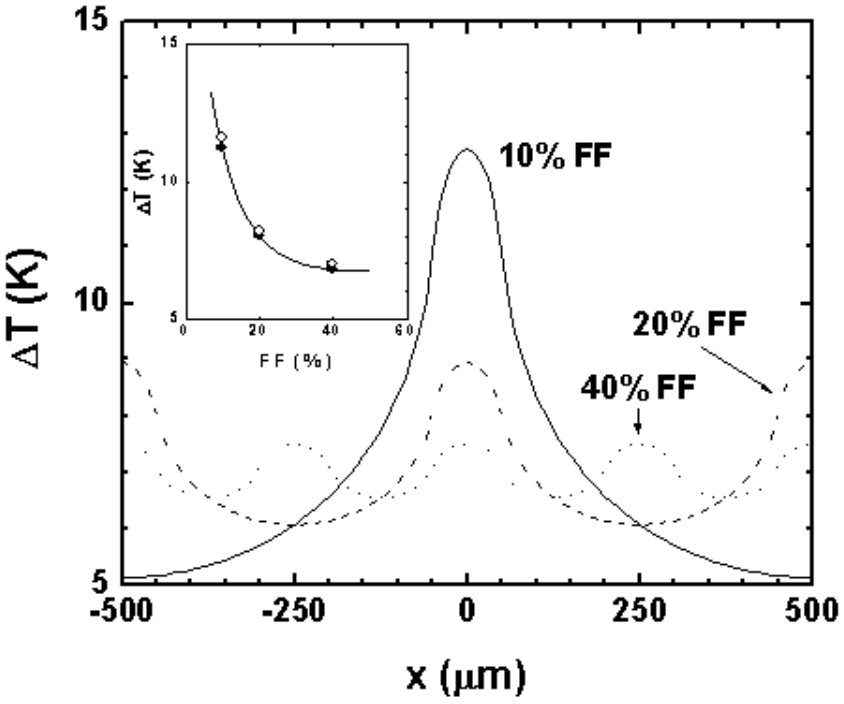

FIG. 21: Active-region temperature distribution over 1 mm of a 1cm long laser bar with different fill factors at the total dissipated power of 20 W. The inset demonstrates the analytical (solid symbols) and experimental (open symbols) average temperature change for different FFs at given total dissipated power of 20 W.

comparing the temperature distribution within the slotted-BeO geometry with the corresponding data calculated for the planar model. The specific requirement for both geometries was the equivalence of the maximum bar temperature with 100% fill factor. Figure 21 shows the analytically calculated temperature distribution of a 1-mm section of a 10-mm laser bar for fill factors of 10%, 20%, and 40%, at 20 W total dissipated power per bar. As the fill factor goes up the temperature goes down in the regions close to the emitters, due to decreasing the dissipated power per stripe, and goes up in the regions between emitters, due to increasing mutual heating between adjacent emitters. The temperature distribution becomes more ho-

mogenous along the bar with increasing FF, reducing the influence of fill factor on the thermal resistance. In the inset of Figure 21 we compared the analytic results for average active region temperature rise versus fill factor with the experimental results, and found good agreement. In agreement with experimental results, our calculations show that a further fill-factor increase ($f > 40\%$) does not lead to significant reduction of overheating.

E. Conclusion

In this chapter

- We report on the development of high-power diode arrays operating near 1.5 μm. A 25-W cw output power was obtained from a 1D array at 16 ^{o}C, and 110-W qcw power was obtained from a 2D array at 18 ^{o}C.

- Diode laser linear arrays emitting at 2.3-μm output 10-W cw and 18.5-W qcw (30μs/300 Hz). The array peak wall-plug efficiency was near 9%.

- In steady-state operation the thermal resistance decreases with increased fill factor; however, this dependency saturates at high FFs. The good agreement between the theoretical and experimental results shows that the analytical model developed in the chapter III D is adequate to determine the temperature distribution in the laser arrays.

V. TRANSIENT THERMAL ANALYSIS OF HIGH-POWER DIODE LASER ARRAYS WITH DIFFERENT FILL FACTORS

A. Introduction

The high heat dissipation in the laser arrays makes effective thermal management a critical issue for reliable and efficient operation. In section IV B we considered the InP-based laser arrays designed for resonant pumping of erbium doped solid state lasers [43]. The optical pumping scheme requires high power sources that can reliably provide a large fraction of their output energy in relatively narrow erbium absorption bands. The erbium fluorescence lifetime of about 5-10 ms favors relatively long pump-laser pulses [15–17]. The long current-injection pulses produce a considerable temperature increase within the diode laser structure that induces a red-shift of the output wavelength. The thermal drift of laser array emission spectra can lead to misalignment with erbium absorption bands. Pump-laser power falling outside these bands cannot be absorbed and is wasted, deteriorating the pumping efficiency. The reliability of pumping arrays is one more important issue for solid state laser systems. Laser array degradation mechanisms are enhanced by high operational temperatures, and aging tests indicate that the laser array lifetime decreases exponentially with active region temperature [72]. Another key parameter for optically pumped solid state laser systems is the output power of the pumping diodes, which is known to saturate with temperature. In recent years, many groups optimized the design of laser arrays to decrease the thermal load and maximize the output power in different operating regimes [6, 77, 83]. It was shown

that arrays with high emitter density (large fill factor) are preferred for short-pulse high peak power operation [5, 84], while arrays with low emitter density (small fill factor) are better suited for long-pulse, high average power operation [11, 12]. For efficient near-resonant pumping of erbium solid-state lasers the design of the laser bars and package architecture should minimize the active-region temperature rise, and hence, minimize the pump-laser spectral red-shift throughout the long-pulse duration. A comprehensive thermal analysis of the packaged laser arrays provides a powerful tool for the design optimization. The steady-state temperature distributions in semiconductor laser diodes were evaluated from numerical [13] and analytical [49, 85, 86] solutions of the heat conductance equation with different boundary conditions. In section IV D and [43, 70] the temperature distribution was obtained for laser diode bars in cw mode operation. The transient thermal response of high power LDAs was studied experimentally [62, 71] and theoretically [70, 73] for laser bars with planar heat spreaders. In this chapter we consider the effect of laser bar design on transient temperature change for laser bars mounted in bar-in-groove heat spreaders. A good agreement between the theoretical modeling and the experimental results was demonstrated.

In section V B, the laser bar design and the heating kinetics measurements are discussed. The description of theoretical model is presented in section V C. Section V D discusses the experimental results and their comparison with the analytical model.

B. Device structure and experimental technique

The InGaAsP/InP laser structure emitting at 1.5-μm was grown by metalloorganic chemical vapor deposition. The active region contains three InGaAsP quantum wells (QWs). The broadened waveguide (710 nm) was incorporated between n- and p-clad layers, each 1.5-μm thick. The total thickness of the laser bar structure including the substrate was 140 μm. The 100-μm-wide, 1-mm-long laser stripes were equally spaced along the 1-cm-wide laser bar and were separated by unpumped regions. The laser bars with 10%, 20%, and 40% fill factors (FF) were fabricated. These bars were mounted onto metallized grooves in 2-mm-thick BeO heat spreaders bonded to water-cooled microchannel heat sinks; see the the Figure 13. Details of the laser heterostructure and bar design were considered in chapters IV B and II B and in Ref.[43, 44]. The laser diode arrays with different FFs showed a threshold current density of 480 A/cm^2 and a slope efficiency of 0.5 W/A in the linear part of the light-current characteristic at room temperature.

The temperature kinetics in the active region was determined by measuring the temporal evolution of the laser spectra during a 400-ms current pulse. The pulse duration was chosen to be long enough to reach a steady-state operation regime. The spectrum evolution was measured using a 0.5-m grating monochromator equipped with a linear 256-pixel InGaAs photodetector. The photodetector array captured the laser array spectrum with a resolution of 0.16 nm without rotating the diffraction grating. The total full-width at half-maximum (FWHM) spectral width for the arrays was typically around 10 - 15 nm, while single emitters cleaved from the same

wafer exhibit a typical FWHM spectral width of 5 nm. The coupling of the laser emission into the monochromator was performed using an integrating sphere. The emission spectra was recorded every 100 ms during the current pulse. Recording all the spectra during a single current pulse ensured highly accurate measurements. For a quantitative characterization of the spectrum red-shift with time during the current pulse, we computed the weighted average [71] wavelength of each emission spectrum and subtracted the weighted average wavelength of the emission spectrum measured at the beginning of the pulse.

Figure 22 shows the weighted average wavelength shift and the average active-region temperature change for the 20% FF array at drive currents of 30, 40, and 50 A. A conversion coefficient between the wavelength shift and the active-region temperature was obtained by measuring the laser spectral shift under low-duty cycle (0.02%), short-pulse (200 ns) operation at a variety of heat sink temperatures. The heating kinetics was measured for arrays with 10%, 20%, and 40% FF over a wide range of total dissipated power. Figure 23 shows the temperature change divided by the bar dissipated power for arrays with different FFs. The total dissipated power P_{dis} equals the difference between the input electrical power and the output optical power. The data show that the active-region temperatures (for the same dissipated power) in arrays with 10%, 20%, and 40% FF are significantly different during the first few hundred microseconds. The temperature difference between the 20% and 40% FF arrays diminishes over time, while the 10% FF array demonstrates higher temperatures for all times. This steady-state thermal behavior correlates the thermal resistances of the arrays determined in Ref. [43].

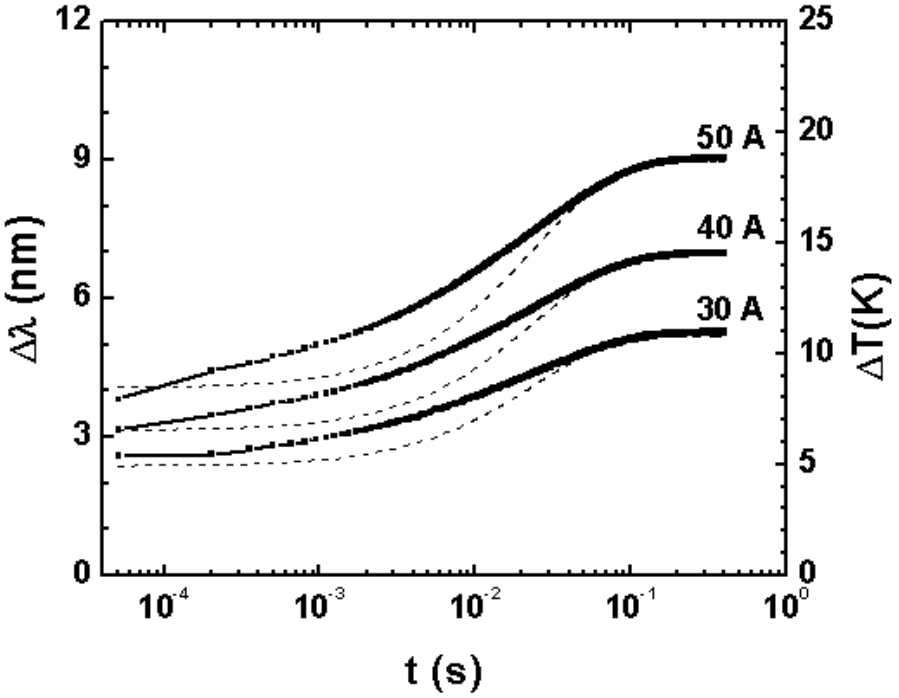

FIG. 22: Time dependence of average wavelength shift (left axis) and the corresponding active region temperature change (right axis) for a laser diode array with a 20% fill factor.

C. Theory

1. Vertical geometric model

To describe the transient active-region thermal behavior of laser arrays, we developed an analytical model including the main features of the laser array assembly. The schematic cross section of the array assembly considered in the model is shown in Figure 24.

The BeO heat spreader occupies the region $0 < y < b$ and isothermally contacts an ideal heat sink at $y = b$. The bottom edge ($y = 0$) of the heat spreader is adiabatically isolated. The thickness of the heat spreader is at least one order of

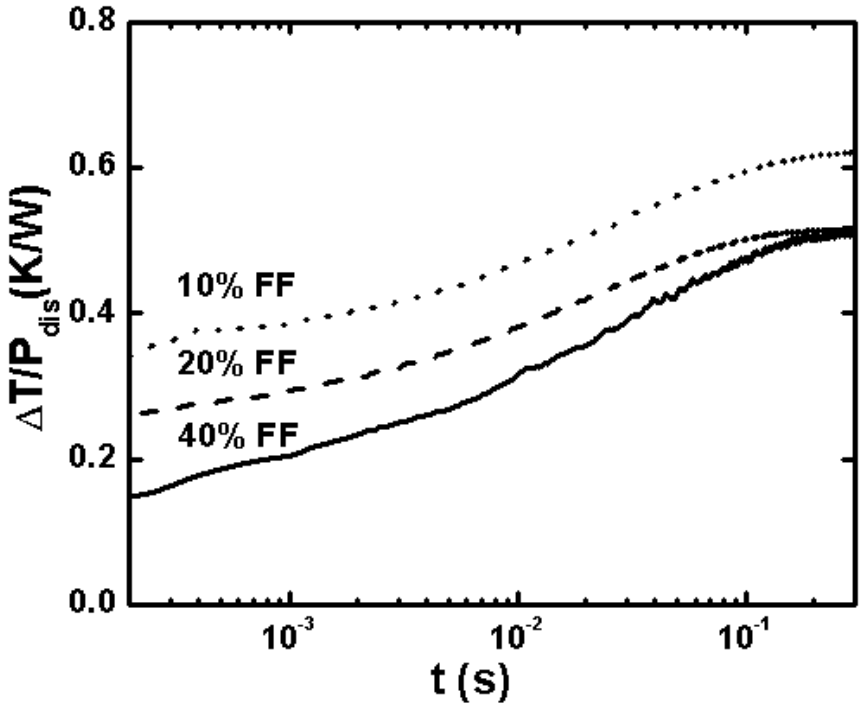

FIG. 23: Active region temperature rise divided by dissipated power (i.e. thermal resistance) as a function of time for different FF arrays.

magnitude larger than the thickness of the laser bar. Because of this, we neglect the thickness of the laser bar, which can be represented by a homogeneous heat source located at $x = 0$, $0 < y < a$ and shown in Figure 24 by the line AB. The heat conductance problem is reduced to the solution of the equation

$$\frac{\partial T}{\partial t} = \chi \left(\frac{\partial^2 T}{\partial x^2} + \frac{\partial^2 T}{\partial y^2} \right), \tag{5.1}$$

in the region $x > 0$, $0 < y < b$ with boundary conditions

$$\kappa \left. \frac{\partial T}{\partial y} \right|_{y=0} = 0 \ , \tag{5.2a}$$

$$\kappa \left. \frac{\partial T}{\partial x} \right|_{x=0} = -Q\theta(a - y) \ , \qquad a < b \ , \tag{5.2b}$$

$$T|_{y=b} = 0 \ , \tag{5.2c}$$

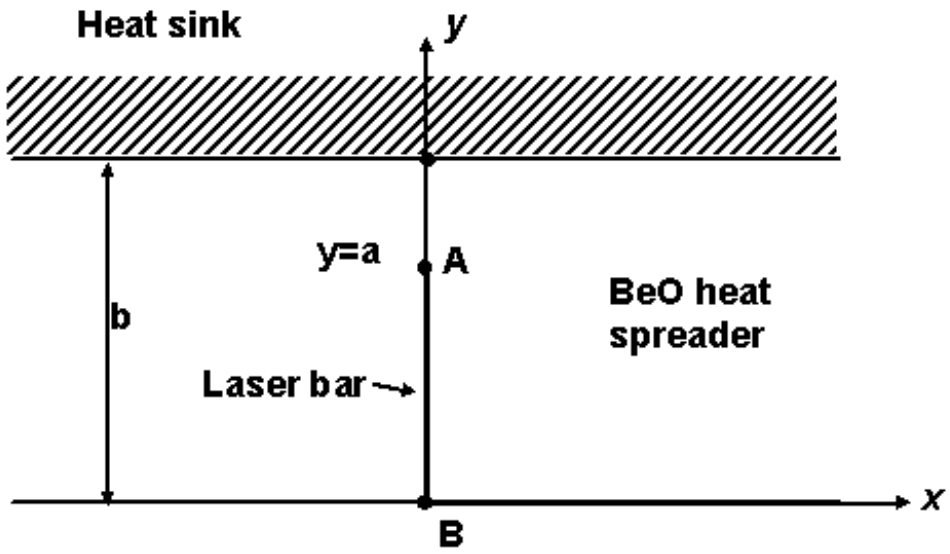

FIG. 24: The cross section geometry of the laser array assembly used for the calculation of the temperature distribution is shown. The BeO heat spreader occupies the region $0 < y < b$. The laser bar is plotted by the line A-B. The interface between the BeO heat spreader and the heat sink lies at $y = b$.

and the initial condition

$$T|_{t=0} = 0 \ . \tag{5.3}$$

where T is the temperature change due to heating, χ and κ are the BeO thermal diffusivity and conductivity, respectively, and Q is the heat flux density from the laser structure. Due to the symmetry of the problem, we consider only the region $x > 0$. The equation is solved using the Laplace transformation. The equation is solved using the Laplace transformation (Appendix V F), and the result is after the inverse Laplace transformation

$$T(x,y,t) \ = \ \frac{4Q\sqrt{\chi}}{\pi\kappa}\sum_{n=0}^{\infty}\frac{1}{2n+1}\sin\frac{\pi(2n+1)a}{2b}\ \cos\frac{\pi(2n+1)y}{2b}$$
$$\times\frac{1}{2\pi i}\int_{\delta-i\infty}^{\delta+i\infty}\frac{\exp\left[pt - x\sqrt{p+(2n+1)^2/\tau}/\sqrt{\chi}\right]}{p\sqrt{p+(2n+1)^2/\tau}}\ dp \tag{5.4}$$

where $\tau = 4b^2/\pi^2\chi$ - is the relaxation time. The contour integral can be reduced to a definite one with the help of the expansion in poles of the integrand,

$$T(x,y,t) \;=\; T_0(x,y) - \frac{16Qb}{\pi^3\kappa}\sum_{n=0}^{\infty}\frac{1}{2n+1}\; e^{-(2n+1)^2t/\tau}\sin\frac{(2n+1)\pi a}{2b}\;\cos\frac{(2n+1)\pi y}{2b} \times\int_0^{-\infty} e^{-r^2t/\tau}\left[\frac{\cos\left(\pi r^2 x/2b\right)}{r^2+(2n+1)^2}\right]\; dr\;, \tag{5.5}$$

where

$$T_0(x,y) = \frac{8bQ}{\pi^2\kappa}\sum_{n=0}^{\infty}\frac{1}{(2n+1)^2}\; e^{-\pi(2n+1)x/2b}\sin\frac{(2n+1)\pi a}{2b}\;\cos\frac{(2n+1)\pi y}{2b} \tag{5.6}$$

is the steady-state temperature.

For comparison with our experimental results, we computed the average temperature change. The temperature averaged over the stripe was defined as

$$\overline{T}(t) \;\equiv\; \frac{1}{a}\int_0^a T(0,y,t)dy \tag{5.7}$$

In the comparison of our theoretical calculation with the experimental results we were interested mainly on the functional dependence of the temperature on time and not on the absolute value of the temperature, which is dependent on physical parameters known with some uncertainty. As such, we treated the prefactor $16Qb/\pi^3\kappa$ in Eqs.(5.5) as an adjustable parameter chosen to fit the computed results at large time to the experimentally determined steady-state temperature rise.

2. Three heating periods

The real geometry is more complicated than the geometry considered in the theoretical model due to the finite thickness of the laser bar, a nonuniform heat source

distribution in the bar, and the nonideality of the water-cooled heat sink. The first two factors are important in the short-time scale and the last one affects the estimation of the relaxation time τ, which describes longer-time-scale heating. The heating of the laser bar structure controls the initial active-region temperature rise. The heat is generated in the active regions under the metal stripe contacts and produces heat fluxes. The propagation of heat fluxes from the InP-based laser bar structure to the BeO heat spreader is hindered by the In-based solder layer serving as interface between these materials and the smaller value of thermal diffusivity of InP ($\chi_1 = 0.37\ \ cm^2/s$) in comparison with BeO ($\chi = 0.9 cm^2/s$). During the initial period of heating, lateral heat spreading and heating of the laser bar occurs. The duration of this period τ_1 can be estimated as l_1^2/χ_1, where $l_1 \sim 100\mu m$ is a characteristic length on the order of the thickness of the laser bars and the separation between adjacent stripes in the laser bar. The initial heating of the laser bar structure was included in our model by assuming that the measurement starts with time delay $t_0 \approx \tau_1$ after the beginning of the current pulse. The analytically calculated heating kinetics is shown by the dashed lines in Figure 22 for the 30-, 40-, and 50-A drive currents.

The analytical model describes the heating at $t > \tau_1$ after the entire laser bar has been heated and the nonuniformity of the heat source distribution is diminished. In this time range ($t > \tau_1$) it is possible to separate two periods when the temperature kinetics given by Eqs.(5.5) can be greatly simplified. In the short-time kinetics $t << \tau$, i.e., the second period of heating, a simplified form of the solution can be obtained directly from Eqs.(5.28) and (5.7), where the condition $t << \tau$ corresponds

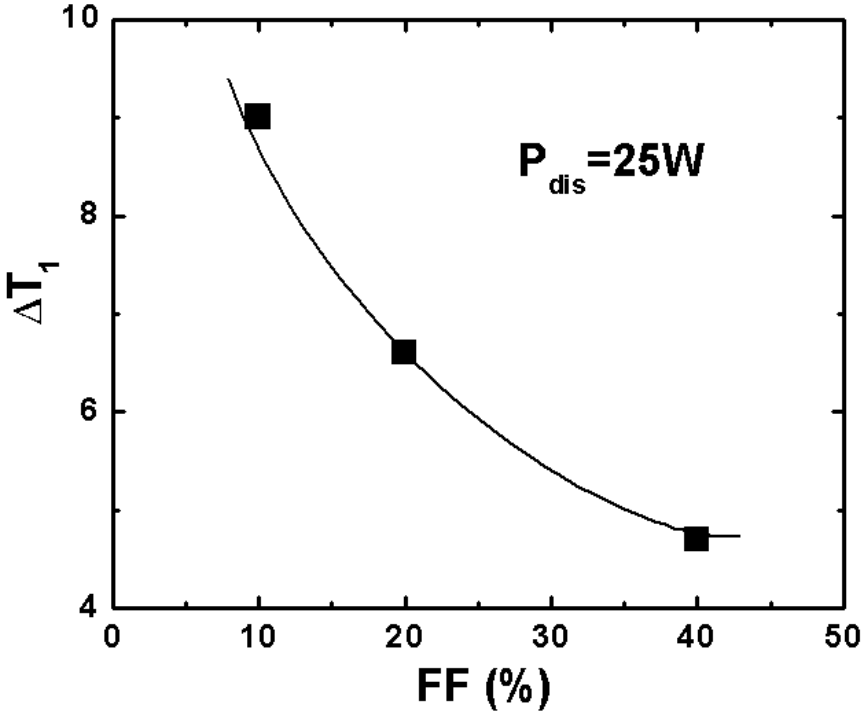

FIG. 25: The Active-region initial temperature rise during the first 200 mus for 10%, 20%, and 40% FF arrays at a constant total bar P_{dis} of 25 W.

to $pt >> 1$. This gives

$$\overline{T}(t) \;=\; \frac{2Q\sqrt{\chi t}}{\kappa\sqrt{\pi}} \tag{5.8}$$

The third period of heating is the long-time kinetics when $t >> \tau$. In this period, the rapid decay of the exponential terms make it possible to approximate the temperature change using just one term ($n = 0$) from the sum obtained by substituting Eq.(5.5) and (5.7).

$$\overline{T}(t) \;=\; \overline{T_0}\left(1 - \sqrt{\frac{\tau}{\pi t}}s^{-t/\tau}\right), \tag{5.9}$$

where

$$\overline{T_0} = \frac{8bQ}{\pi^2\kappa}\frac{2b}{\pi a}\sin^2\left(\frac{\pi a}{2b}\right) \tag{5.10}$$

In summary, the heating process can be subdivided into three time periods, each with different heat transport conditions. During the first period, the active-region temperature increase of laser arrays is determined by heating the structure very close to the laser stripes. As the first period progresses, the heat fluxes from individual laser stripes overlap, producing a nearly uniform heat flux. In the second period the unified heat flux propagates through the BeO heat spreader toward the cooler, but the substantially heated region is still much smaller than the thickness of the heat spreader. The heating kinetics is determined by Eq.(5.8) and the temperature change of the active region is proportional to the square-root of time. In the third period the heat flux has reached the heat sink, the entire BeO heat spreader is heated, and the active-region temperature asymptotically approaches its steady-state value, Eq.(5.9).

D. Results and discussion

To study the initial heating ($t \leq \tau_1$) of laser arrays with different fill factors, the active-region temperature rise sDT1d was measured for the first 200 μs. Figure 25 demonstrates the dependence of T_1 on FF at 25-W total dissipated power per bar. The experimental results show that the temperature rise during the first 200 μs is highest for the array with a 10% FF and smallest for the array with 40% FF. In the first heating period the active-region heating is mainly determined by the power dissipation in each stripe. The dissipated power per stripe scales with the number of stripes for a constant total dissipated power in the bars. At a given dissipated power in the bar, the temperature rise decreases with the fill factor. This decrease

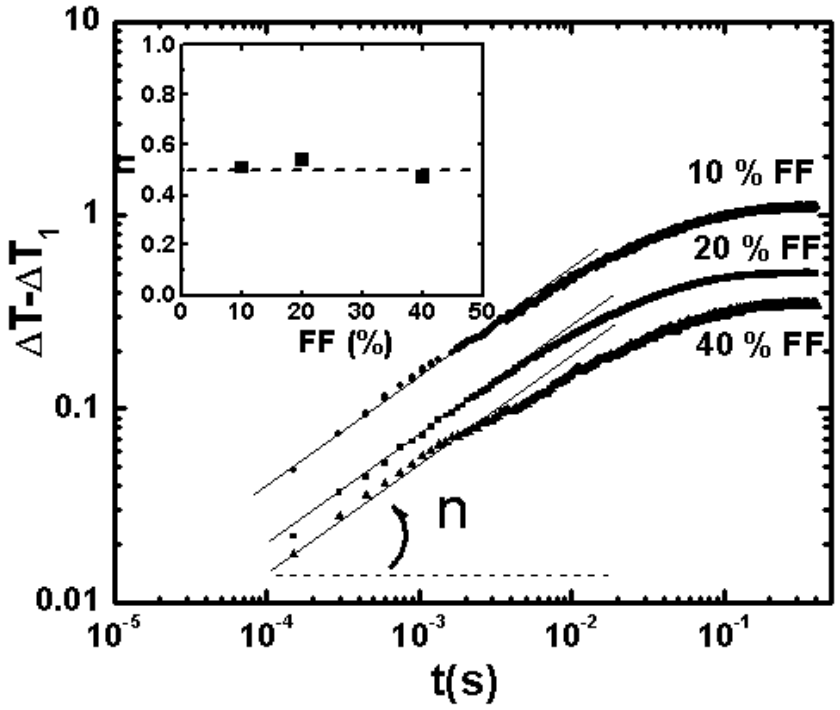

FIG. 26: The temperature changes are plotted on double-log axes for the three fill factors. The solid lines were fitted to the experimental data over the time interval of 200 μs to 10 ms. The computed slopes are shown in the inset as a function of the fill factor.

is not directly proportional to the number of stripes. During the first 200 μs, the active-region temperature increases are 9 K for 10% FF, 6.5 K for 20% FF, and 4.5 K for 40% FF at 25-W dissipated power per bar. This is an evidence of the lateral heat transport in the laser bar structure that is responsible for the mutual heating of the adjacent emitters. This lateral heat transport leads to an overlapping of heat fluxes from the active-region areas under the metal contacts and to the homogenization of the temperature distribution in the laser bar.

The second period lasts while $\tau_1 < t \ll \tau$ ends before the heat flux reaches the heat sink. Since in the first period the heat fluxes from under the stripe areas

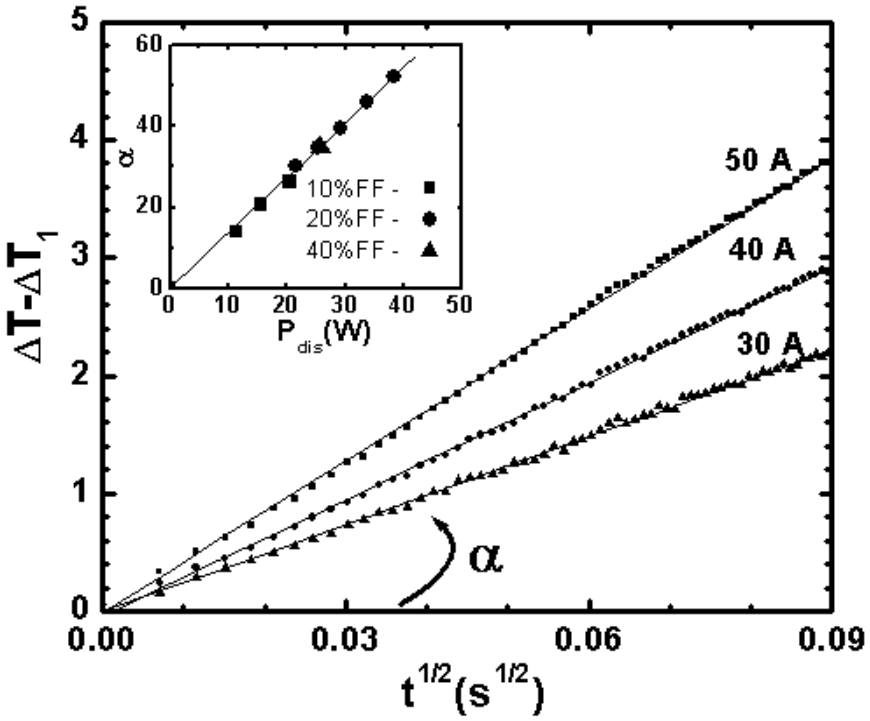

FIG. 27: The active-region temperature change of a 20% fill factor array is plotted vs the square-root of time with 30-, 40-, and 50-A drive currents at a coolant temperature of 18 ^{o}C. The dependency of the slope coefficient α the total dissipated power is shown for 10% (square symbol), 20% (circle symbol), and 40% (triangle symbol) fill factor arrays in the inset.

have merged into a nearly uniform flux, the thermal kinetics is expected to be independent of the distance between emitters (i.e., fill factor) in this second phase of heating. To analyze the active-region temperature change during the second period, the initial temperature rise (T_1) was subtracted from the measured active-region temperature. Figure 26 shows the temperature change on double-log axes for arrays with the three different fill factors. The solid lines in Figure 26 were fitted to the experimental data over the time interval from 200 μs to about 10 ms. The inset shows the computed slopes as a function of the fill factor. The slope of these fit lines is close to 0.5, indicating that the active-region temperature change increases

as the square-root of time. Figure 27 shows the active-region temperature change versus the square-root of time for a 20% fill factor array at 30-, 40-, and 50-A drive currents, which corresponds to 21.5-, 29-, and 38.5-W total dissipated power. The temperature dependencies are well approximated by straight lines with the slope coefficient a. The measured slope coefficients have been plotted in the inset for 10%, 20%, and 40% FF arrays as functions of the total dissipated power. The slope coefficient increases linearly with the total dissipated power at the same rate for all three arrays. This shows that over the time scale $\tau_1 < t \ll \tau$ the temperature kinetics is determined by the free propagation of the nearly uniform heat flux in the BeO heat spreader and does not depend on the fill factor. This thermal behavior is well described by the asymptotic analytical solution of Eq.(5.8).

In the third period ($t \gg \tau$), the active-region temperature change approaches the steady-state value (T_0) with a characteristic time constant τ and is characterized by long-time asymptotic kinetics given by Eq.(5.9). Equation (5.9) can be rewritten as

$$\frac{[T_0 - T(t)]}{T_0} \;=\; \sqrt{\frac{\tau}{\pi t}}\exp(-t/\tau). \tag{5.11}$$

For $t \gg \tau$, the exponential time dependence dominates the preceding term $\sqrt{\tau/\pi t}$, and Eq. (5.11) can be simplified as

$$\frac{[T_0 - T(t)]}{T_0} \;\sim\; exp(-t/\tau). \tag{5.12}$$

In Figure 28 the normalized difference between the active-region temperature change and the experimentally determined steady-state temperature rise (T_0) is plotted in semilogarithmic scale for all three arrays. Figure 5 shows that for long times, $t > 20ms$, the data are well approximated by the exponential time dependence

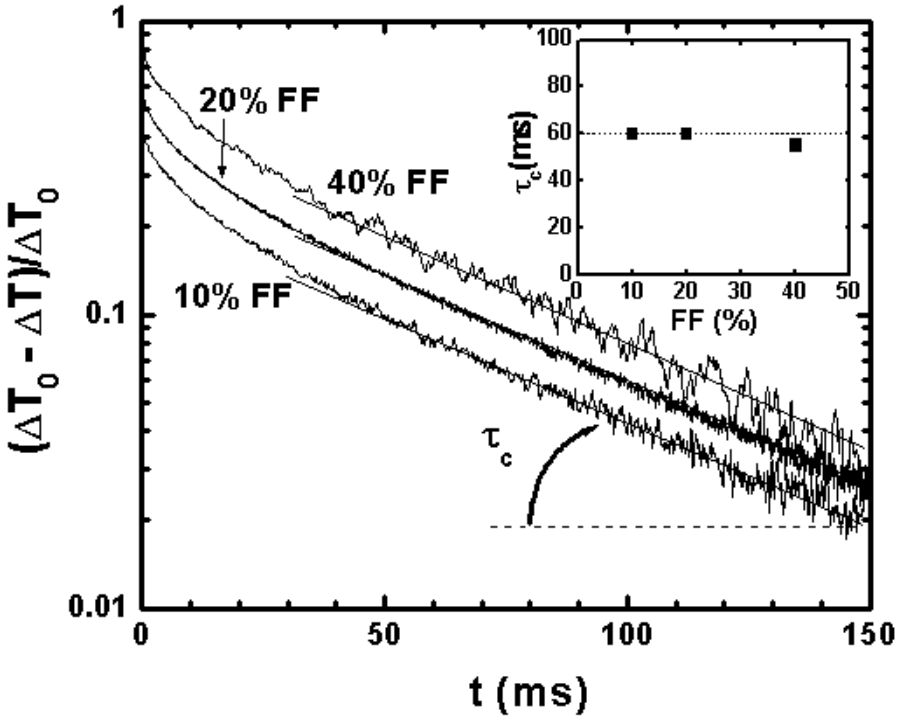

FIG. 28: Normalized deviation from steady-state temperature vs time is plotted for arrays with 10%, 20%, and 40% FF. The slopes of the solid lines are used to calculate τ_c, which is shown in the inset.

given by Eq.5.12). The slopes of the solid lines in Figure 28 were fitted to the data to calculate the experimental time constant τ_c, which is shown in the inset as a function of FF. The long-time heating kinetics of these arrays with different FFs can be characterized with the same τ_c of about 60 ms. The experimental time constant τ_c is larger than the theoretically calculated time constant, $\tau \approx 20ms$. The reason for the discrepancy is that the theoretical model describes only the heat propagation through the heat spreader, while in reality there are other factors affecting the temperature kinetics, such as the nonideality of the water-cooled heat sink and the interface between the BeO heat spreader and the heat sink.

E. Conclusion

In this chapter

- We report on the experimental and theoretical study of heating kinetics for InGaAsP/InP arrays with 10%, 20%, and 40% fill factors. The transient heating process can be divided into three time periods; each period is determined by its own heat transport condition. During the first period, the bar structure is heated and the heat fluxes from individual stripes of the laser bar overlap, producing the nearly uniform heat flux. The duration of this period s (τ_1) is determined by the geometry of the laser bar and its thermal diffusivity. The second period is characterized by the propagation of the nearly uniform heat flux through the BeO heat spreader. The heat propagation length for the second period is much smaller than the heat spreader thickness. By the third period the heat flux has reached the heat sink, the entire heat spreader has been heated, and the temperature distribution approaches the steady state.

- The theoretical model describes the heating in the second and the third heating periods. In the second period the active-region temperature change of laser arrays is proportional to the square-root of time, and in the third period the deviation of the temperature from its steady-state value decreases exponentially with time. The initial temperature rise is included in the model by assuming a time delay ($t_0 \approx \tau_1$) to heat the laser bar structure.

- The temperature rise measured for the first 200 μs is dependent on the power dissipated per stripe and the distance between stripes. This initial tempera-

ture change decreases with the fill factor for a given total bar power dissipation and bar size. The second and third periods are well described by the asymptotic solutions of the theoretical model. The maximal difference between the analytically predicted temperature and the experimental one is about two degrees for the largest current, 50 A. This small difference indicates that our model adequately describes the array heating process. The discrepancy between the theoretical and experimental values of the time constant t in the third heating period shows that the thermal properties of the interfaces and the nonideality of the heat sink substantially affect the heat flow.

F. Appendix (Vertical geometric model)

The problem is to solve the equation

$$\frac{\partial T}{\partial t} = \chi \left(\frac{\partial^2 T}{\partial x^2} + \frac{\partial^2 T}{\partial y^2} \right) , \tag{5.13}$$

in the region $x > 0$, $0 < y < b$ with boundary conditions

$$\kappa \left. \frac{\partial T}{\partial y} \right|_{y=0} = 0 , \tag{5.14a}$$

$$\kappa \left. \frac{\partial T}{\partial x} \right|_{x=0} = -Q\theta(a-y) , \qquad a < b , \tag{5.14b}$$

$$T|_{y=b} = 0 , \tag{5.14c}$$

and the initial condition

$$T|_{t=0} = 0 . \tag{5.15}$$

After the Laplace transform,

$$\Theta(x,y) = \int_0^\infty e^{-pt} T(x,y,t) dt , \tag{5.16}$$

the problem is reduced to the equation

$$\chi \left(\frac{\partial^2 \Theta}{\partial x^2} + \frac{\partial^2 \Theta}{\partial y^2} \right) = p\Theta , \tag{5.17}$$

with boundary conditions

$$\kappa \left. \frac{\partial \Theta}{\partial y} \right|_{y=0} = 0 , \tag{5.18a}$$

$$\kappa \left. \frac{\partial \Theta}{\partial x} \right|_{x=0} = -\frac{Q}{p}\, \theta(a-y) , \qquad a < b , \tag{5.18b}$$

$$\Theta|_{y=b} = 0 , \tag{5.18c}$$

The problem Eqs.(5.17) and (5.18) is equivalent to

$$\frac{\partial^2\Theta}{\partial x^2}+\frac{\partial^2\Theta}{\partial y^2}-\frac{p}{\chi}\,\Theta=0\ , \tag{5.19}$$

in the stripe $-b<y<b$ with the boundary conditions

$$\Theta(x,\pm b)=0\ , \qquad \kappa\,\frac{\partial\Theta}{\partial x}\bigg|_{x=0}=-\frac{Q}{p}\,\theta(a-|y|) \tag{5.20}$$

The solution can be represented in the form

$$\Theta(x,y)=\sum_{n=0}^{\infty}\Theta_n(x)\cos\frac{\pi(2n+1)y}{2b}\ . \tag{5.21}$$

Then

$$\Theta_n(x)=\frac{1}{b}\int_{-b}^{b}\Theta(x,y)\cos\frac{\pi(2n+1)y}{2b}\,dy\ , \tag{5.22}$$

that leads to the equation

$$\frac{d^2\Theta_n}{dx^2}-\left[\frac{p}{\chi}+\frac{\pi^2(2n+1)^2}{4b^2}\right]\Theta_n=0 \tag{5.23}$$

with the boundary condition

$$\frac{d\Theta}{dx}\bigg|_{x=0}=-\frac{Q}{\kappa p}\,\frac{4}{\pi(2n+1)}\,\sin\frac{\pi(2n+1)a}{2b}\ . \tag{5.24}$$

The solution to this equation that goes to zero at $x\to\infty$ is

$$\begin{aligned}\Theta_n(x)\ =\ &\frac{Q}{\kappa p}\,\frac{4}{\pi(2n+1)}\,\sin\frac{\pi(2n+1)a}{2b}\left[\frac{p}{\chi}+\frac{\pi^2(2n+1)^2}{4b^2}\right]^{-1/2}\\ &\times\exp\left\{-\left[\frac{p}{\chi}+\frac{\pi^2(2n+1)^2}{4b^2}\right]^{1/2}x\right\}.\end{aligned} \tag{5.25}$$

The substitution in Eq.(5.21) gives

$$\begin{aligned}\Theta(x,y)\ =\ &\frac{4Q\sqrt{\chi}}{\pi\kappa p}\sum_{n=0}^{\infty}\frac{\exp\left[-x\sqrt{p+(2n+1)^2/\tau}/\sqrt{\chi}\right]}{(2n+1)\sqrt{p+(2n+1)^2/\tau}}\,\sin\frac{\pi(2n+1)a}{2b}\\ &\times\cos\frac{\pi(2n+1)y}{2b}\ ,\end{aligned} \tag{5.26}$$

where

$$\frac{1}{\tau} = \frac{\pi^2 \chi}{4b^2} \ . \tag{5.27}$$

After the inverse Laplace transformation

$$\begin{aligned} T(x,y,t) \ &= \ \frac{4Q\sqrt{\chi}}{\pi\kappa} \sum_{n=0}^{\infty} \frac{1}{2n+1} \sin\frac{\pi(2n+1)a}{2b} \ \cos\frac{\pi(2n+1)y}{2b} \\ &\qquad \times \frac{1}{2\pi i} \int_{\mathcal{L}} \frac{\exp\left[pt - x\sqrt{p+(2n+1)^2/\tau}/\sqrt{\chi}\right]}{p\sqrt{p+(2n+1)^2/\tau}} \ dp \\ &= \ T_0(x,y) + \frac{4Q\sqrt{\chi}}{\pi\kappa} \sum_{n=0}^{\infty} \frac{1}{2n+1} \ e^{-(2n+1)^2 t/\tau} \sin\frac{\pi(2n+1)a}{2b} \ \cos\frac{\pi(2n+1)y}{2b} \\ &\qquad \times \frac{1}{2\pi i} \int_{(0+)}^{-\infty} \frac{\exp\left(pt - x\sqrt{p/\chi}\right)}{p-(2n+1)^2/\tau} \ \frac{dp}{\sqrt{p}} \ , \end{aligned} \tag{5.28}$$

where

$$T_0(x,y) = \frac{8bQ}{\pi^2\kappa} \sum_{n=0}^{\infty} \frac{1}{(2n+1)^2} \ e^{-\pi(2n+1)x/2b} \sin\frac{\pi(2n+1)a}{2b} \ \cos\frac{\pi(2n+1)y}{2b} \tag{5.29}$$

The contour integral can be transformed to a definite one,

$$\begin{aligned} &\frac{1}{2\pi i} \int_{(0+)}^{-\infty} \frac{\exp\left(pt - x\sqrt{p/\chi}\right)}{p-(2n+1)^2/\tau} \ \frac{dp}{\sqrt{p}} = \\ &\quad = \frac{1}{2\pi i} \left[\int_{\infty}^{0} \frac{\exp\left(-rt + ix\sqrt{r/\chi}\right)}{-r-(2n+1)^2/\tau} \ \frac{-dr}{-i\sqrt{r}} + \int_{0}^{\infty} \frac{\exp\left(-rt - ix\sqrt{r/\chi}\right)}{-r-(2n+1)^2/\tau} \ \frac{-dr}{i\sqrt{r}} \right] \\ &\quad = -\frac{1}{\pi} \int_0^{\infty} e^{-rt} \frac{\cos(x\sqrt{r/\chi})}{r+(2n+1)^2/\tau} \frac{dr}{\sqrt{r}} \ . \end{aligned} \tag{5.30}$$

Finally,

$$\begin{aligned} T(x,y,t) \ &= \ T_0(x,y) - \frac{16bQ}{\pi^3\kappa} \sum_{n=0}^{\infty} \frac{1}{2n+1} \ e^{-(2n+1)^2 t/\tau} \sin\frac{\pi(2n+1)a}{2b} \ \cos\frac{\pi(2n+1)y}{2b} \\ &\qquad \times \int_0^{\infty} e^{-r^2 t/\tau} \frac{\cos(\pi r^2 x/2b)}{r^2+(2n+1)^2} \ dr \end{aligned} \tag{5.31}$$

The asymptote of the integral is

$$\int_0^\infty e^{-r^2 t/\tau} \, \frac{dr}{r^2 + (2n+1)^2} = \begin{cases} \dfrac{\pi}{2(2n+1)} \ , & t \ll \tau \ , \\ \dfrac{\sqrt{\pi\tau/t}}{2(2n+1)^2} \ , & t \gg \tau \ . \end{cases} \tag{5.32}$$

The temperature averaged over the stripe is defined as

$$\overline{T}(t) \equiv \frac{1}{a} \int_0^a T(0,y,t) dy \tag{5.33}$$

One form of the average temperature is obtained from Eq.(5.28),

$$\begin{aligned} \overline{T}(t) \ &= \ \frac{4Q\sqrt{\chi}}{\pi\kappa} \ \frac{2b}{\pi a} \sum_{n=0}^\infty \frac{1}{(2n+1)^2} \sin^2 \frac{\pi(2n+1)a}{2b} \\ &\qquad \times \frac{1}{2\pi i} \int_{\mathcal{L}} e^{pt} \ \frac{dp}{p\sqrt{p + (2n+1)^2/\tau}} \ . \end{aligned} \tag{5.34}$$

The other form is obtained from Eq.(5.31),

$$\begin{aligned} \overline{T}(t) \ &= \ \overline{T}_0 - \frac{16bQ}{\pi^3\kappa} \ \frac{2b}{\pi a} \sum_{n=0}^\infty \frac{1}{(2n+1)^2} \ e^{-(2n+1)^2 t/\tau} \sin^2 \frac{\pi(2n+1)a}{2b} \\ &\qquad \times \int_0^\infty e^{-r^2 t/\tau} \ \frac{dr}{r^2 + (2n+1)^2} \ , \end{aligned} \tag{5.35}$$

where

$$\overline{T}_0 = \frac{8bQ}{\pi^2\kappa} \ \frac{2b}{\pi a} \sum_{n=0}^\infty \frac{1}{(2n+1)^3} \ \sin^2 \frac{\pi(2n+1)a}{2b} \ . \tag{5.36}$$

The asymptotical behavior at large t follows from Eq.(5.35),

$$\overline{T}(t) \ = \ \overline{T}_0 - \frac{8bQ}{\pi^3\kappa} \ \frac{2b}{\pi a} \ \sin^2 \frac{\pi a}{2b} \sqrt{\frac{\pi\tau}{t}} \ e^{-t/\tau} \ , \qquad t \gg \tau \ . \tag{5.37}$$

The opposite limit, $t \ll \tau$, follows from Eq.(5.34),

$$\begin{aligned} \overline{T}(t) \ &= \ \frac{4Q\sqrt{\chi}}{\pi\kappa} \ \frac{2b}{\pi a} \sum_{n=0}^\infty \frac{1}{(2n+1)^2} \sin^2 \frac{\pi(2n+1)a}{2b} \frac{1}{2\pi i} \int_{\mathcal{L}} e^{pt} \ \frac{dp}{p^{3/2}} \\ &= \ \frac{4Q\sqrt{\chi}}{\pi\kappa} \ \frac{2b}{\pi a} \ \frac{2\sqrt{t}}{\sqrt{\pi}} \ \frac{1}{2} \sum_{n=0}^\infty \frac{1}{(2n+1)^2} \left[1 - \cos \frac{\pi(2n+1)a}{b} \right] \\ &= \ \frac{4Q\sqrt{\chi t}}{\pi^{3/2}\kappa} \ \frac{2b}{\pi a} \ \frac{\pi}{4} \ \frac{\pi a}{b} = \frac{2Q\sqrt{\chi t}}{\sqrt{\pi}\kappa} \ . \end{aligned} \tag{5.38}$$

[1] P. Crump, J. Wang, T. Crum, S. Zhang, M. Grimshaw, W. Dong, M. DeFranza, S. Das, M. DeVito and J. Farmer, Proceedings of the 18th Solid State and Diode Laser Technology Review, Los Angeles, USA, Paper Diode 1-5 4 (2005).

[2] P. Crump, J. Wang, T. Crum, S. Das, M. DeVito, W. Dong, J. Farmer, Y. Feng, M. Grimshaw, D. Wise, S. Zhang, in Proceedings of Photonics West, High-Power Diode Laser Technology and Applications III, San Jose, USA, volume SPIE 5711 (2005).

[3] H.G.Treusch, A. Ovtchinnikov, X. He, M. Kanskar, J. Mott, S. Yang, IEEE J. Sel. Top. Quantum Electron., **6** 601 (2000)

[4] M. Sakamoto, J. G. Endriz, and D. R. Scifres, Electron. Lett., **28**, 197, (1992).

[5] J. A. Skidmore, B. L. Freitas, C. E. Reinhardt, E. J. Utterback, R. H. Page, and M. A. Emanuel, IEEE Photonics Technol. Lett. **9**, 1334 (1997).

[6] S. A. Payne, R. J. Beach, C. Bibeau, C. A. Ebbers, M. A. Emanuel, E. C. Honea, C. D. Marshall, R. H. Page, K. I. Schaffers, J. A. Skidmore, S. B. Sutton, and W. F. Krupke, IEEE J. Sel. Top. Quantum Electron. 3, **71** (1997).

[7] M. D. Rotter, B. Bhauchu, K. Cutter, S. Gonzales, R. Merrill, S. Mitchell, C. Parks and Yamamoto, Proceeding of the Solid State and Diode Laser Technology Review, SSDLTR-04, Sys-1, 2004.

[8] S. R. Bowman, S. O'Connor, S. Biswal, Proceeding of the Solid State and Diode Laser Technology Review, SSDLTR-04, SS2-2, 2004.

[9] M. Kanskar, T. Earles, T.J. Goodnough, E. Stiers, D. Botez, L.J. Mawst , Electron.

Lett., **41**, 245 (2005)

[10] M. Kanskar, Photon. Spectr., 39 (1): 112 JAN 2005

[11] M .Maiorov, R. Menna, V. Khalfin, H. Milgazo, R. Matarese, D. Garbuzov, and J. Connolly, IEEE Photonics Techn. Lett. **11**, 961 (1999)

[12] M. Maiorov, R. Menna, V. Khalfin, H. Milgazo, A. Triano, D. Garbuzov and J. Connolly, Electron. Lett. **35**, 636 (1999).

[13] A. Bärwolff, R. Puchert, P. Enders, U. Menzel, D. Ackermann, J. Therm. Anal. **45**, 417 (1995).

[14] S. D. Setzler, P. A. Budni, and E. P. Chicklis, OSA Trends Opt. Photonics Ser. **50**, 309 (2001).

[15] S. D. Setzler, P. A. Budni, and E. P. Chicklis, in *Advanced Solid-State Lasers*, OSA Trends in Optics and Photonics Vol. 50, edited by Christopher Marshall (Optical Society of America, Washington, DC, 2001), p. 309.

[16] S. D. Setzler, K. J. Snell, T. M. Pollak, P. A. Budni, Y. E. Young, and E. P. Chicklis, Opt. Lett. **28**, 1787 (2003).

[17] S. D. Setzler, M. P. Francis, Y. E. Young, J. R. Konves, and E. P. Chicklis, IEEE J. Quantum. Electron., **11** (2005)

[18] D. Garbuzov, I. Kudryashov, M. Dubinskii, Appl. Phys. Lett., **86**, 131115 (2005)

[19] D. Garbuzov, I. Kudryashov, M. Dubinskii, Appl. Phys. Lett., **87**, 121101 (2005)

[20] L. Shterengas, G. L. Belenky, J. G. Kim, and R. U. Martinelli, Semicond. Sci. Technol., **19**, 655 2004.

[21] J. G. Kim, L. Shterengas, R. U. Martinelli, G. L. Belenky, D. Z. Garbuzov, and W.

K. Chan, Appl. Phys. Lett., vol. **81**, 3146 (2002).

[22] J. G. Kim, L. Shterengas, R. U. Martinelli, and G. L. Belenky, Appl. Phys. Lett., **83**, 1926 (2003).

[23] G. W. Turner, H. K. Choi, and M. J. Manfra, Appl. Phys. Lett., **72**, 876 (1998).

[24] D. Z. Garbuzov, H. Lee, V. Khalfin, R. Martinelli, J. C. Connolly, and G. L. Belenky, IEEE Photon. Technol. Lett., **11**, 794 (1999).

[25] G. Belenky, J. G. Kim, L. Shterengas, R. U. Martinelli, and D. Garbuzov, 18th IEEE Int. Semiconductor Laser Conf. Kongresshaus Garmisch-Partenkirchen, Garmisch, Germany, Sept. 29Oct. 3, 2002.

[26] Y. Cuminal, A. N. Baranov, D. Bec, P. Grech, M. Garcia, G. Boissier, A. Joullie, G. Glastre, and R. Blondeau, **14**, 283 (1999).

[27] Y. Rouillard, A. Perona, A. Salhi, P. Grech, F. Chevrier, C. Alibert, M. Garcia, C. Becker, X. Marcadet, and C. Sirtori, Proc. MIOMD-V, Annapolis, MD, Sept. 811, 2002, pp. 181182.

[28] C. Mermelstein, S. Simanowski, M. Mayer, R. Kiefer, J. Schmitz, M. Walther, and J. Wagner, Appl. Phys. Lett., **77**, 1581 (2000).

[29] M. Grau, C. Lin, and M.-C. Amann, IEEE Photon. Technol. Lett., **16**, 383 (2004).

[30] A. Ongstad and R. Kaspi, J. Appl. Phys., **92**, 5621 (2002).

[31] X. He, D. Xu, A. Ovtchinnikov, F. Malarayap, R. Supe, S.Wilson, and R. Patel, Electron. Lett., **35**, 397 (1999).

[32] J. S. Major, J. S. Osinski, and D. F.Welch, Electron. Lett., **29**, 2112 (1993).

[33] J. N.Walpole, H. K. Choi, L. J. Missaggia, Z. L. Liau, M. K. Connors, G. W. Turner,

M. J. Manfra, and C. C. Cook, IEEE Photon. Technol. Lett., **11**, 1223 (1999).

[34] A.P. Ongstad, R. Kaspi, J.R. Chavez, G.C. Dente, M.L. Tilton, D.M. Gianardi, J. Appl. Phys. **92**, 5621 (2002).

[35] J.R. Meyer, C.A. Hoffman, F.J. Bartoli, L.R. Ram-Mohan, Appl. Phys. Lett., **67**, 757 (1995).

[36] I. Vurgaftman, J.R. Meyer, L.R. Ram-Mohan, J. Appl. Phys., **89**, 5815 (2001).

[37] R. Kaspi, A. Ongstad, G.C. Dente, J. Chavez, M.L. Tilton, D. Gianardi, Appl. Phys. Lett., **81**, 406 (2002).

[38] C. Lin, M. Grau, O. Dier, and M.-C. Amann, Appl. Phys. Lett., **84**, 5088 (2004).

[39] M. Grau,C. Lin, O. Dier, C. Lauer, and M.-C. Amann, Appl. Phys. Lett., **87**, 241104 (2005).

[40] D. Garbuzov, L. Xu, S.R. Forrest, R. Menna, R. Martinelli, J.C. Connolly, Electron. Lett., **32**, 1717 (1996).

[41] L. Shterengas, R. Menna, C. W. Trussell, D. Donetsky, G. Belenky, J. Connolly, D. Garbuzov, J. Appl. Phys. **88**, 2211 (2000).

[42] G. Belenky, L. Shterengas, C. W. Trussell, C. L. Reynolds, M. S. Hybertsen, R. Menna, *Future Trends in Microelectronics*, edited by S. Luryi, J. Xu, and A. Zaslavsky (IEEE, New York, 2002), p. 230.

[43] A. Gourevitch, G. Belenky, D. Donetsky, B. Laikhtman, D. Westerfeld, C. W. Trussell, H. An, Z. Shellenbarger, R. Martinelli, Appl. Phys. Lett. **83**, 617 (2003).

[44] D. Z. Garbuzov, R. J. Menna, R. U. Martinelli, J. H. Abeles, and J. C. Connolly, Electron. Lett. **33**, 1635 (1997).

[45] G. Erbert, A. Bärwolff, J. Sebastian, and J. Tomm, "High-power broad-area diode lasers and laser bars", in *High-Power Diode Lasers*, edited by R. Diehl, Lasers, Topics Appl. Phys. **78**, 173 (2000) (Springer-Verlag, Berlin, Heidelberg, 2000).

[46] D. Botez and D. R. Scifres (editors), *Diode Laser Arrays* (Cambridge University Press, Cambridge, 1994).

[47] N. W. Carlson, *Monolithic Diode-Laser Arrays* (Springer-Verlaf, Berlin, Heidelberg, 1994)

[48] W. B. Joyce and S. W. Wemple, J. Appl. Phys. **41**, 3818 (1970)

[49] W. B. Joyce and R. W. Dixon, J. Appl. Phys. **46**, 856 (1975).

[50] W. B. Joyce and R. W. Dixon, J. Appl. Phys. **14**, 1981 (1975).

[51] H. Yonezu, I. Sakuma, K. Kobayashi, T. Kamejima, M. Ueno, and Y. Nannichi, Japan J. Appl. Phys. **12**, 1585 (1973).

[52] W. P. Dumke, Solid-State Electron. **16**, 1279 (1973).

[53] J. Buus, IEEE J. of Quantum Electron., **QE-15**, 734 (1979).

[54] W. Streifer, R. D. Burnham, and D.R.Scifres, IEEE J. Quantum Electron. **QE-18**, 856 (1982).

[55] G. Lengyel, P. Meissner, E. Patzak, and K.-H. Zschauer, IEEE J. of Quantum Electron., **QE-18**, 618 (1982).

[56] D. P. Wilt and A. Yariv, IEEE J. Quantum Electron., **QE-17**, 1941 (1981).

[57] W. B. Joyce, J. Appl. Phys. **51**, 2394 (1980).

[58] G. P. Agrawal, J. Appl. Phys. **56** 3100-3109 (1984).

[59] R. Papannareddy, W.E.Ferguson, Jr., and J. K. Butler, IEEE J. Quant. Electron.

QE-24, 60 (1988).

[60] B. Laikhtman, A. Gourevitch, D. Donetsky, D. Westerfeld, and G. Belenky, J. Appl. Phys. **95**, 3880 (2004).

[61] W. B.Joyce andd R. W. Dixon, J. Appl. Phys. **46**, 855 (1974).

[62] A. Gourevitch, B. Laikhtman, D. Westerfeld, D. Donetsky, G. Belenky, C. W. Trussell, Z. Shellenbarger, H. An, R. U. Martinelli, J. Appl. Phys., **97**, 084503-1, (2005).

[63] R. P. Sarzala, W. Nakwaski, J. Therm. Anal. **36**, 1171 (1990); J. Therm. Anal. **39**, 1297 (1993).

[64] Z. Nehari, *Conformal mapping* (Dover Publication, Inc., New York, 1952).

[65] A. Lavrentev i B. V. Shabat, *Metody teorii funktsii kompleksnogo peremennogo*, Moskva : Gos. izd-vo fiziko-matematicheskoi lit-ry, 1958; German ed.: M.A.Lawrentjew und B.W. Schabat. Methoden der komplexen Funktionentheorie., (bersetzung: Udo Pirl, Reiner Khnau [und] Lothar v. Wolfersdorf.) Berlin, Deutscher Verlag der Wissenschaften, 1967. Series title: Mathematik fr Naturwissenschaft und Technik Bd. 13, Mathematik fr Naturwissenschaft und Technik Bd. 13.

[66] F. D. Gakhov, *Boundary Value Problems* (Dover Publications, Inc., New York 1966).

[67] P. M. Smowton and P. Blood, Appl. Phys. Lett., **70**, 1073 (1997).

[68] L. Shterengas, G. L. Belenky, A. Gourevitch, D. Donetsky, J. G. Kim, R. U. Martinelli, and D. Westerfeld, IEEE Photon. Technol. Lett., **16**, 2218 (2004)

[69] M. Kim, W. W. Bewley, J. R. Lindle, C. S. Kim, I. Vurgaftman, J. R. Meyer, J. G. Kim, and R. U. Martinelli, Appl. Phys. Lett., **83**, 5374 (2003).

[70] B. Laikhtman, A. Gourevitch, D. Westerfeld, D. Donetsky and G. Belenky, Semicond. Sc. Technol., **20**, 1087 (2005).

[71] M. Voss, C. Lier, U. Menzel, A. Barwolff, and T. Elsaesser, J. Appl. Phys. **79**, 1170 (1996).

[72] M. Fukuda, Reliability and Degradation of Semiconductor Lasers and LEDs (Boston, MA: Artech House, 1991).

[73] R. Puchert, A. Barwolff, M. Voss, U. Menzel, J. W. Tomm, and J. Luft, IEEE Trans. Compon., Packag. Manuf. Technol., Part A **23**, 95 (2000)

[74] A. Knauer, G. Erbert, H. Wenzel, A. Bhattacharya, F. Bugge, J. Maege, W. Pitroff, and J. Sebastian, Electron. Lett. **35**, 638 (1999)

[75] J.K. Wade, L.J. Mawst, D.Botez, and J.A. Morris, Electron. Lett. **34**, 1100 (1998)

[76] Al-Muhanna, L.J. Mawst, D. Botez, D.Z. Garbuzov, R.U. Martinelli, and J.C. Connolly, Appl. Phys. Lett. **73**, 1182 (1998)

[77] J. G. Endriz, M. Vakili, G. S. Browder, M. DeVito, J.M. Haden, G. L. Harnagel, W. E. Plano, M. Sakamoto, D. F. Welch, S. Willing, D. P. Worland and H. C. Yao, IEEE J. Quantum Electron., **28** 952 (1992)

[78] M. Jansen, P. Bournes, P. Coryni, F. Fang, M. Finander, M.Hmelar, T. Johnston, C. Jordan, R. Nabiev, J. Nightingale, M. Widman, H. Asonen, J. Aarik, A. Salokatve, J. Nappi and K. Rakennus, Optics Express , **4**, 3 (1999)

[79] X. He, S. Srinivasan, V. Zarate, R. Patel, Semiconductor Laser Conference, 1998. ISLC 1998 NARA. 1998 IEEE 16th International , pp. 123 -124

[80] S. Gupta, A. Garcia, S. Srinivasan, X. He, S. Wilson, J. Harrison, R. Patel, Semi-

conductor Laser Conference, 1998. ISLC 1998 NARA. 1998 IEEE 16th International , pp. 53 -54

[81] X. He, M. Ung, S. Srinivasan, R. Patel, Electron. Lett. **33**, 1221 (1997)

[82] D. V. Donetsky, G. L. Belenky, D. Z. Garbuzov, H. Lee, R. U. Martinelli, G. Taylor, S. Luryi, and J. C. Connolly, Electron. Lett., **35**, 298 (1999).

[83] R. Beach, W. J. Benett, B. L. Freitas, D. Mundinger, B. J. Comaskey, R. W. Solarz, and A. Emanuel, IEEE J. Quantum Electron. **28**, 966 (1992).

[84] H. Q. Le, G. W. Turner, and J. R. Ochoa, IEEE Photonics Technol. Lett. **10**, 663 (1998).

[85] M. Ito and T. Kimuro, IEEE J. Quantum Electron. **17**, 787 (1981).

[86] B. Laikhtman, A. Gourevitch, D. Donetsky, D. Westerfeld, and G. Belenky, J. Appl. Phys. **95**, 3880 (2004).